energies

MDPI

Article

A Recycling Pathway for Rare Earth Metals (REMs) from E-Waste through Co-Gasification with Biomass

A. S. M. Sazzad Parveg [1], Ramin Ordikhani-Seyedlar [2], Tejasvi Sharma [1], Scott K. Shaw [2] and Albert Ratner [1,*]

[1] Department of Mechanical Engineering, University of Iowa, Iowa City, IA 52242, USA
[2] Department of Chemistry, University of Iowa, Iowa City, IA 52242, USA
* Correspondence: albert-ratner@uiowa.edu; Tel.: +1-319-384-0883

Abstract: This manuscript investigates an improvised gasification process for capturing and recycling rare earth metals (REMs) from consumer and industrial electronic wastes, often termed "e-waste". The proposed procedure is based on the formation of coalesced and aggregated metal nodules on biochar surfaces through the gasification of e-waste mixed with gasifier feedstocks. A preliminary understanding of metal nodule formation based on different atmospheric conditions (inert, oxidizing, and oxidizing followed by reducing atmospheres) was examined in both pilot-scale gasifier and tube furnace experiments using iron powder mixed with corn. Iron powder is representative of the REM in the e-waste. Metal nodule sizes, morphology, and composition are analyzed and compared via scanning electron microscopy (SEM), energy dispersive X-ray spectroscopy (EDS), and X-ray fluorescence spectroscopy (XRF) techniques. We conclude that sintering is the key mechanism responsible for metal nodule growth through metal particle coalescence and aggregation by migration and diffusion of metal particles on biochar surfaces at elevated temperatures. Oxidizing atmosphere followed by a reducing atmosphere facilitates larger metal nodule growth compared to only an inert or oxidizing atmosphere. Additionally, the effect of adding NaCl salt is investigated on lowering the metal nodules' surface energy and enhancing both metal particle and metal nodule agglomeration characteristics. Salt addition facilitates spherical metal nodule formation without any significant effect on the nodule composition and localized formation of nodules.

Keywords: rare earth metals (REMs); gasification; biomass; electronic wastes; rare earth metals (REMs) recycling

Citation: Parveg, A.S.M.S.; Ordikhani-Seyedlar, R.; Sharma, T.; Shaw, S.K.; Ratner, A. A Recycling Pathway for Rare Earth Metals (REMs) from E-Waste through Co-Gasification with Biomass. *Energies* **2022**, *15*, 9141. https://doi.org/10.3390/en15239141

Academic Editors: Lin Ma, Xin Yang and Hao Zhou

Received: 31 October 2022
Accepted: 29 November 2022
Published: 2 December 2022

1. Introduction

The demand for rare earth metals (REMs) is growing rapidly, owing to their crucial role in technologies including electronics, metal alloys, magnets, batteries, light emitting diodes, and smart materials (Figure 1) [1]. REMs are a set of 17 heavy metals comprising 15 lanthanides (La-Lu), Scandium (Sc), and yttrium (Y). The scarcity of economically feasible REM mines, high extraction costs, and expensive and environmentally taxing purification processes have raised concerns for industries that rely on these materials. Such concerns have placed REMs in the critical or strategic element listings [2]. The rapidly growing market demand for these materials exacerbates challenges in supply. For example, global production of REMs in 2021 was around 280,000 metric tons which is a 15% increase from the previous year [3]. China leads in both REMs reserves (35%) and production (60%) globally [3].

The scarcity of operational/economical REMs mines and refineries has led to supply chain risks, driving sustainable and environmentally friendly methods to recycle these metals from consumer and industrial waste streams. However, REM recycling is challenged by limitations of available technology to extract REMs economically and responsibly from consumer products and industrial wastes. As such, less than 1% of REMs are being recycled

in end-of-life consumer products [4] while approximately 75% of all aluminum [5] and about 40% of all steel produced is created through recycling [6].

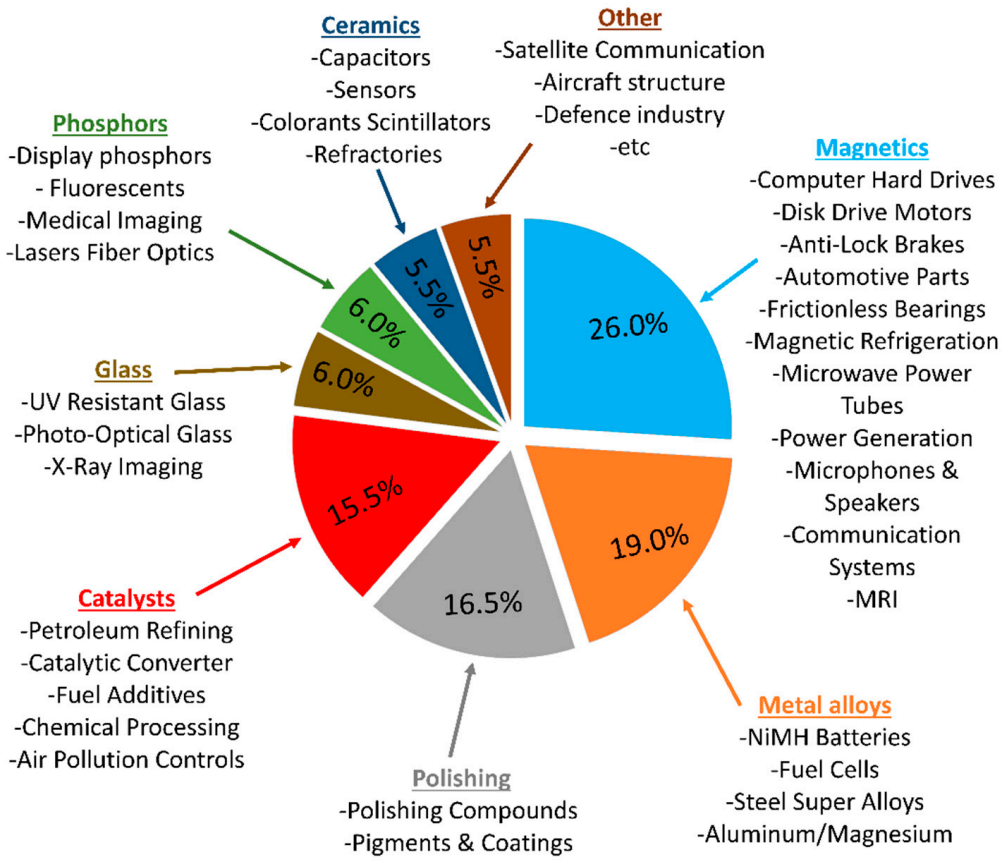

Figure 1. Rare earth metals applications in different sectors globally [1].

Conventional REM extraction is carried out via aqueous acid leaching from raw minerals, followed by biphasic solvent extraction. This is resource and pollution-intensive and resulted in a degrative environmental cost of USD 14.8 billion in 2015, urging the scientific community to search for an environment-friendly and sustainable solution [7]. Within this context, REM recycling from industrial and consumer waste has become a topic of interest. Additional sources might include coal fly ash, bauxite residue, pre-consumer scrap, and e-waste from consumer electronics and electric vehicles. Two key approaches (Figure 2) for REM's recycling include (1) direct recycling of pre-consumer manufacturing REM scrap/residues, and (2) urban mining of post-consumer EOL products/e-waste [8–14]. Globally, the e-waste production rate is around 40 million tons/year and less than 20% of this e-waste is recycled [15]. In addition to these benefits of recycling, it is important to consider that mining additional REMs also leads to the so-called "balance problem" wherein work to extract a less earth-abundant and critically important REM (e.g., neodymium) generally also yields excessive production of more abundant REMs (e.g., cerium) [16]. This unbalances the supply and demand of REMs. Recycling feedstocks typically contain more desirable ratios of REMs, so recapturing these metals will both lower the total amount of mined ores and mitigate imbalanced supply and demand trends. However, recycling REMs through e-waste is a complicated process due to the lack of public awareness of the environmental and economic benefits of e-waste and REMs recycling, the lack of tech waste recycling facility, the lack of structural and process framework for separate collection with source segregation, pre-processing and recycling of e-waste, lack of economic incentive and legislation, inflexibility in the equipment/component design to recycling efficiently and effectively challenging the cost-effective recovery, and need of technological and process

innovation to recycle REMs from e-waste with nominal energy requirement and optimized process time with minimal impact on the environment as well as human health. In addition, e-waste contains complex mixtures of metals, multi-element alloys, and polymetallic structures which poses a challenge to developing an efficient REMs recovery process [17]. Table 1 shows a list of REMs containing e-waste components with their respective sources.

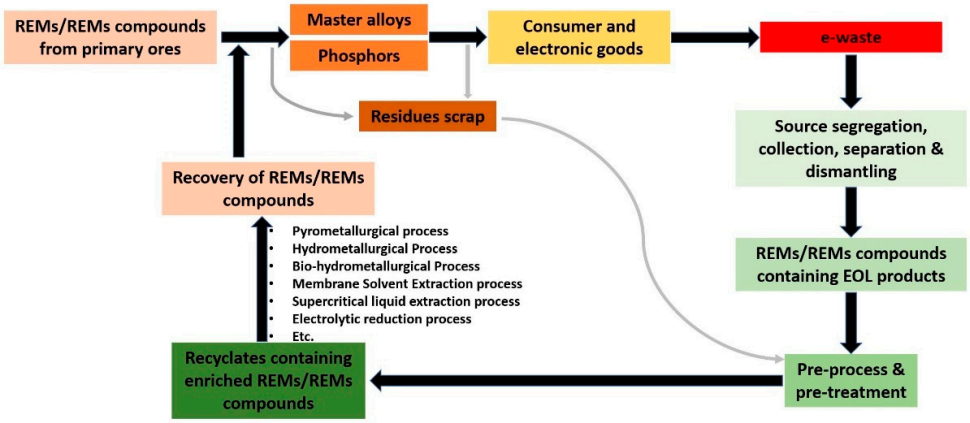

Figure 2. Simplified pathways to recycle REMs/REMs compounds from e-waste.

Table 1. List of e-waste components containing REMs with respective sources [4,18–22].

E-Waste Components	Sources	Present REMs
Permanent NdFeB magnets	-Automobiles (small magnets such as motors, switches, sensors, actuators, etc.) -Mobile phones (loudspeakers, switches, microphones, etc.) Hard disk drives -Computers (cooling fans, switches, drive motors, etc.) -Consumer electronic devices (kitchen utensils, electric shavers, etc.) -Industrial electric motors -Electric vehicles -Wind turbine generators -SmCo magnets (electric motors, NMR spectrometers, etc.)	Neodymium (Nd) Dysprosium (Dy) Praseodymium (Pr) Terbium (Tb) Gadolinium (Gd) Samarium (Sm)
Phosphors	-Fluorescent lamps -LEDs -LCD backlights -Plasma screens -Cathode-ray tubes	Europium (Eu) Terbium (Tb) Yttrium (Y) Cerium (Ce) Gadolinium (Gd) Lanthanum (La)
Nickel metal hydride batteries	-Rechargeable batteries -Electric vehicle batteries	Lanthanum (La) Cerium (Ce) Neodymium (Nd) Praseodymium (Pr) Yttrium (Y)

Metallurgical science plays an important role in the recycling of REMs from end-of-life (EOL) consumer products or e-waste as most established methods are based on different metallurgical technologies [4,19–21,23–32]. REMs containing e-waste or EOL consumer products are typically preprocessed to generate "recyclates" having a higher concentration of REMs. These recyclates are then further processed to extract REMs for reuse. Hydrometallurgical methods involve strong acids (sulfuric acid, nitric acid, hydrochloric acid) to leach base metals, and complex chemical reagents (cyanide, halide, thiourea, thiosulfate, etc.), to leach out the REMs from e-waste or EOL products [19,21,23,26,33,34]. The main drawbacks of hydrometallurgical techniques are the high consumption of chemical

reagents, the generation of a high volume of effluents, and the generation of a variety of hazardous and toxic by-products [23,35]. These by-products and effluents can adversely impact the environment as well as be hazardous to human health [21,23,26,33]. Another technique is the pyrometallurgical recovery method where e-waste or EOL products are treated at elevated temperatures in a furnace (blast furnace, plasma arc furnace, etc.), to generate metal-rich residue (~70%), oil (~23%) and gases (~5%) [21,23,26,33]. Pyrometallurgical methods are expensive, energy-intensive, and can generate toxic gases such as dioxins and furans [21,23,26,33]. Another promising technique is the bio-hydrometallurgical method which is commonly referred to as bioleaching where micro-organisms, such as bacteria, archaea, and fungi, are utilized to dissolve metals instead of applying chemical reagents [3,23,35,36]. Bio-hydrometallurgical method's advantages include low operational cost, low energy requirements, and low environmental and health impacts [23,33,35,36]. However, the limitations of bio-hydrometallurgical methods include lengthy process time, difficulty in controlling bio-reactions, and the technology is still under development. Research initiatives are going on to find the most optimized method for REMs recovery from e-waste/EOL in terms of low process time, low energy intensive, and minimal environmental and health impact. Other methods for REMs recycling from e-waste may include the gas phase extraction method [37,38], supercritical liquid extraction method [26,39,40], mechanical activation and leaching [26], electrolytic reduction method [26,39,40], membrane solvent extraction method [25,41], vacuum induction melting, hydrolysis and magnetic separation (VIM-HM) method [42], electrometallurgical method [43] and flash Joule heating (FJH) method [15]. Comparison and applicability of different recycling methods were investigated extensively and discussed in several review publications [4,27–32,44–49]. Table 2 shows the comparison of different recycling methods of REMs from e-waste/EOL.

Biomass gasification is a sustainable and renewable pathway to produce carbon-neutral energy to address the environmental challenges associated with conventional energy generation processes through fossil fuels. Different biomass feedstocks (corn, soybeans, wood pellets, etc.), and waste-based fuel (e.g., municipal solid waste (MSW), refused derived fuel (RDF), etc.), can be used as gasifier feedstock. The carbon-rich end product, "biochar" is desirable because of its high surface area, porous structure, high cation exchange capacity, and surface functional groups that enable its diverse application in agriculture, water filtration, industrial catalysis support, electronics, building sectors, and in metallurgy [44–46]. Several studies report the effects of different minerals in gasifier feedstocks on biochar characteristics, including details on how these minerals will interact with biochar, the distribution of these minerals on biochar, and how the minerals can evolve morphologically, structurally, and chemically in different processing conditions of gasifier [12,13,44,47]. Sharma et al. observed the formation of localized metal nodules (potassium (K), aluminum (Al), iron (Fe), nickel (Ni), and copper (Cu)) on biochar surfaces from gasifying different biomass (corn grains, soybeans, wood pellets, and RDF), reported their spatial distribution, elemental compositions, and sizes (~25 micron diameter) on biochar surface [12,13,47]. It was suggested that nodule formation might be the result of precipitation and aggregation of metal vapor during gasification. According to Sharma et al., it was proposed that if sufficiently large metal nodule growth can be achieved by optimizing the gasification process conditions and feedstock types, this biochar-containing metal nodule might be further used for metal extraction and metal recycling [12,13,47]. However, aluminum, iron, nickel, and copper had low elemental concentrations (lower than 5% wt.) on the observed nodules. Comparing boiling and melting temperature of the reported metals (boiling temperature: K: 760 °C, Al: 2470 °C, Fe: 2870 °C, Ni: 2800 °C, Cu: 2575 °C, and melting temperature: K: 63 °C, Al: 660 °C, Fe: 1538 °C, Ni: 1453 °C, Cu: 1084 °C), nodule formation through vapor precipitation and aggregation should not be favorable for metals with high boiling temperature as the gasifier operating temperature was around 1000–1200 °C. Thus, there should be an additional mechanism responsible for the presence of aluminum, iron, nickel, and copper on formed nodules. Considering the gasifier's operational steady-state temperature of around 1000–1200 °C (reaction zone), it

can be hypothesized that another possible mechanism of the metal nodule formation might be the sintering of neighboring metal particles/metal composites.

Table 2. Overview of the advantages and disadvantages of the different recycling methods of REMs from e-waste/EOL [17,19,21–24,26,35,36,39,40,50,51].

Technology/Method	Advantages	Disadvantages
Pyrometallurgical	-Minimal chemical consumption -Reusing of energy in upstream or downstream processes	-High energy consumption -Generation of toxic compounds such as dioxins and furans -Gas emissions such as CO2 and CO -Emission of heavy metals, such as lead, arsenic, and cadmium -High capital and operational cost -Feasible only at large scale
Hydrometallurgical	-Short process time -High efficiency on leaching metals -Low energy consumption -Low capital cost -Feasible at smaller scales and expansion is easier	-Expensive sulfur conversion technology -Generation of high volume of effluents -Require high concentration of metals in the e-waste -High chemical consumption -High operational cost
Bio-hydrometallurgical	-Environment friendly -Low operational cost -Low chemical consumption -Low energy consumption -Feasible at smaller scales and expansion is easier	-Less flexibility in controlling bio-reactions -Method is still under development -Long processing time
Mechanical activation and leaching	-Low energy consumption -Low operating cost -High efficiency on leaching metals	-Method is still under development
Supercritical liquid extraction	-Improved extraction efficiency -Low process temperature -No hazardous by-products	-High pressure process -Method is still under development
Electrolytic reduction method	-Low process temperature	-High energy consumption -Generation of toxic gas (chlorine gas)

Sintering is extensively used in the field of powder metallurgy (PM) which can be defined as thermal treatment or a heat treatment process of bonding metal powders, metal particles, or metal powder compacts while they are heated to a temperature between half of the absolute melting temperature to just below the absolute melting temperature, through atomic transport events, by either particle migration and coalescence (simultaneously or alternately by viscous flow, volume diffusion, surface diffusion, grain boundary diffusion) or through Ostwald ripening, or both [48,49,52]. Reduction of the surface atoms' chemical potential is considered the main driver of sintering conditions [53]. In the particle migration and coalescence mechanism (PMC), metal particles migrate on the support surface through Brownian-like motion and collide to form larger particles. In the Ostwald ripening mechanism (OR), individual metal atoms leave one metal particle surface to join another through surface diffusion [54]. As larger particles have lower chemical potentials, the larger particles are more thermodynamically favored for growth at the expense of smaller ones. For smaller particles, the PMC mechanism is dominant while for larger particles OR is the dominant mechanism. Both PMC and OR mechanisms depend on the adhesion energy of metal particles with a support surface, where strong metal support surface interaction facilitates OR and weak metal support surface interaction facilitates PMC [53,55].

The absolute melting temperature of rare earth metals can vary from 795 °C (cerium) to 1663 °C (lutetium) while the absolute boiling temperature can vary from 1196 °C (ytterbium) to 3520 °C (praseodymium). Thus, if the feedstocks contain reasonable amounts of REMs

or REM composites, it can be hypothesized that metallic nodules might form on the biochar surface depending on available metal types as well as the operating conditions of the gasifier (the temperature of the biomass gasification process is usually higher than 700 °C [56–58]. In this regard, pre-processed e-waste, and feedstocks (corn grains, soybeans, wood pellets, MSW, RDF, etc.), might be used together as mixed feedstock for biomass gasifiers. Thus, these REMs containing biochar might be utilized through simple physical separation methods (e.g., centrifugal separation, gravity separation, magnetic separation) to extract REMs from biochar for recycling. To this end, the present work reports an experimental investigation on differentiating the agglomerated or coalesced metal nodule sizes on biochar produced from the gasification of corn mixed with iron (Fe) powder as the target metal. The metal powder content in the biomass feedstock is varied along with the gasifier conditions (oxidizing, inert, reducing atmospheres) to identify favorable conditions for metal nodule growth. The outcomes of this work include suggested pathways for improving nodule growth during gasification, as well as developing a quantitative method to analyze metal recovery efficiency. Our experiments were conducted in a pilot biomass gasifier as well as in a tube furnace. The tube furnace was used to investigate the effects of different atmospheric conditions (oxidizing, inert, reducing atmosphere) on the size of metal nodule formations due to operational limitations regarding varying the atmospheric conditions in the biomass gasifier. Iron powder (Fe powder) was chosen as the target metal powder to simplify the experiments, and also the melting temperature of iron (1538 °C) falls in the higher range of REMs melting temperatures.

Successful implementation of REM's recycling with biomass gasification will improve strategic REMs availability as well as provide the inherent benefits of biomass gasification such as energy generation, sustainable waste processing, and a source of biochar for industrial use. This work provides a preliminary evaluation of a new pathway to recycle REMs. Our goal is to add recycled rare earth metals back to the supply chain to reduce environmental contamination and energy costs from primary mining and separations. Moreover, finding a new approach to recycling REMs would be a positive contribution to the global economy and technology markets [59,60].

2. Materials and Methods

2.1. Materials

Iron (Fe) powder was purchased from the ESPI METALS (−325 Mesh). Corn seed biomass was sourced from local farms in Iowa, US. Gases used here included UHP Ar, a mixture of 95% UHP Ar + 5% HP O_2, a mixture of 95% HP N_2 + 5% HP O_2, and 90% HP N_2 + 10% HP H_2 and were used as received from Linde, US. Table salt (ingredient: sodium chloride, sodium silicoaluminate, dextrose, potassium iodide, sodium bicarbonate) was used as received. Elvacite 2044 was used as received from TALAS as the chemical binding agent for making the pellets.

2.2. Instruments

A Hitachi S-3400N scanning electron microscope (SEM) equipped with a Bruker EDS system was used to take SEM images and elemental mapping from the surface of the biochar samples. A SPEX SamplePrep 8000M Mixer ball mill was used to pulverize the activated carbon and the biochar. A SPEX SamplePrep-3636-115 press machine was used to make pellets for analyzing samples by X-ray fluorescence (XRF). Bulk elemental composition of the samples was determined by a Rigaku ZSX Primus IV XRF instrument. Ag Bio-Power gasification system (Model: B2-250-R) was used for gasification experiments. This is a single-stage downdraft gasifier system which produces syngas (synthesis gas) using various biomass based fuel (e.g., corn grains, soybeans, wood pellets, miscanthus briquettes) or waste-based fuel (e.g., municipal solid waste (MSW), refused derived fuel (RDF), etc.), for the purpose of research by the University of Iowa College of Engineering [12,13]. Gasification inside the tube furnace was performed using a Lindberg HEVI-DUTY 55035-A tube furnace.

2.3. Experimental Methods

2.3.1. Experiments in Biomass Gasifier

The biomass gasification system produces a combustible gas using fuel and air that "co-flows" in the same direction. Figure 3 shows the pilot scale biomass gasifier setup with different key components. The fuel is pyrolyzed on the surface of a reaction zone, where the combustible gases (primarily composed of carbon monoxide—CO, hydrogen—H_2, methane—CH_4, and carbon dioxide—CO_2) are produced [12,13]. Beneath the pyrolysis zone, the fuel is reduced to char and ash. The syngas is pulled through the char reduction zone to exit at an opening near the top of the gasifier. The syngas is transported to a biomass boiler where it is combusted in the boiler's combustion chamber. The driver for the process is the boiler's blower fan which creates a vacuum, causing a draft of air to be drawn down into and through the gasifier. Key sub-systems outside the gasifier are the material handling systems that provide solid fuel(s) and remove by-products (ash and char). There are two metering bins above the gasifier from which solid fuel can be inserted into the system. In the current study, we have used uncoated corn as biomass and iron (Fe) powder as the target metal.

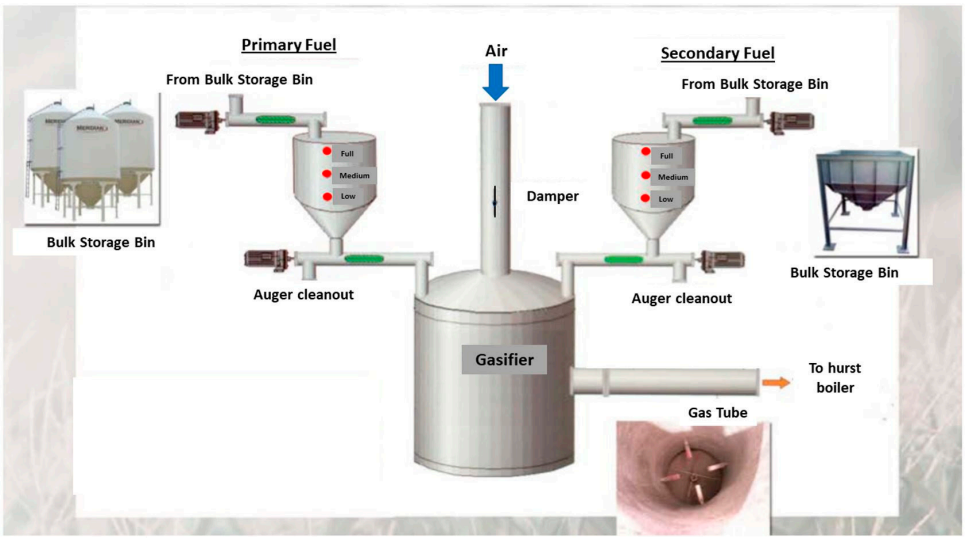

Figure 3. Biomass gasifier setup [12,13].

During the experiment, corn was first fed into the gasifier to start the gasification process. Typically, the gasifier needs around 90–120 min to reach steady-state conditions. In the steady-state condition, the gasifier operates on the negative pressure from the boiler and there is continuous production of synthetic gas which is fed into the boiler. The details of the gasifier operation and gasification process can be found in our previous works [12,13]. Metal powder was dosed into the gasifier after the gasifier reached steady-state temperature (1000–1200 °C). Metal powder was dosed from the top of the gasifier through a customized in-house metal powder dispensing system (based on two ball valve systems (Figure S1a), considering the safety issues as the gasifier operates at an elevated temperature. The dosing system works in three steps to ensure safety (Figure S1b–d). Two ball valves were opened alternatively to dose metal powders and to ensure no outward flow of synthetic gas during dosing. After achieving the steady-state condition, the dosing pipe was adjusted to keep it just above the fuel bed. Then, 4.5 kg of fuel was inserted into the firetube and just after that weighted metal powder (25 g) was dosed into the system. After 15–20 min, the biochar was collected. Then, again, 4.5 kg of fuel was inserted followed by the dosing of metal powder. A total of 50 g Fe powder was dosed with 9 kg of biomass. Biochar was collected in 64 oz glass mason jars. The biochar collected from the gasifier was about 2 kg (20% of the total biomass). SEM and EDS analysis was completed on biochar samples to locate nodule formation or agglomeration of metal particles.

2.3.2. Experiments in Tube Furnace

To better understand the effects of different atmospheric conditions, a set of experiments was conducted in a tube furnace providing a more controlled reaction environment. Figure S2 shows the schematic diagram of the experimental setup with the tube furnace. Before experiments, biomass (corn) with target metal powder (Fe) or salt (NaCl) or both were mixed in a mason jar (32 oz.) by shaking manually according to Table 3 biomass–powder–salt composition (%w/w). The experimental setup was designed to accommodate different atmospheric conditions (oxidizing, inert, reducing atmosphere) by flowing gas through the glass tube during experiment period. First, a certain amount of biomass–metal powder mixture (about 15 g) was weighed and placed on the carrier/boat. The boat was placed inside the glass tube. An exhaust pipe was connected to the cap of the glass tube and submerged in water while the other end was used to flow gases based on desired atmospheric conditions. After achieving the target temperature (inside the furnace), the glass tube was inserted into the tube furnace. In this study, the experiment temperature/target temperature was 1000 ± 100 °C to mimic the temperature condition inside the gasifier. The time duration (residence time) for keeping the glass tube inside the furnace differed based on different experimental conditions (Table 3). After the residence time period, the glass tube was removed from the furnace, and the gas flow was turned off. The carrier/boat was removed from the glass tube and biochar samples were collected. For each run of each atmospheric condition, 15 ± 2 g of biomass with metal powder or biomass with metal powder and salt was used. The biochar samples collected from each run had a mass of 2.50 g ± 0.50 g. For SEM and EDS analysis, approximately 15 g of biochar samples were collected (by running at least six experiments for each atmospheric condition). Four different experimental conditions to mimic different atmospheric conditions were considered, which are listed in Table 3.

Table 3. Different experiment conditions in tube furnace.

Experimental Condition	Biomass–Powder Composition	Atmospheric Condition	Time inside the Furnace (Residence Time)
1	Corn (97.5% by mass) + Fe (2.5% by mass)	100% Ar (Inert atmosphere)	20 s
2	Corn (97.5% by mass) + Fe (2.5% by mass)	95% Ar + 5% O_2 (Oxidizing atmosphere)	20 s
3	Corn (97.5% by mass) + Fe (2.5% by mass)	95% N_2 + 5% O_2 and 90% N_2 + 10% H_2 (Oxidizing followed by reducing atmosphere)	First N_2 + O_2 for 20 s and then N_2 + H_2 for 80 s
4	Corn (95% by mass) + Fe (2.5% by mass) + Salt (2.5% by mass)	95% N_2 + 5% O_2 and 90% N_2 + 10% H_2 (Oxidizing followed by reducing atmosphere)	First N_2 + O_2 for 20 s and then N_2 + H_2 for 80 s

2.4. Data Generation and Analysis Methods

2.4.1. Quantification of Metal Content with Recovery Efficiency on Biochar from Gasifier

X-ray fluorescence (XRF) was used to determine the concentration of the target metals in biochar samples from gasifier. The input metal powder amount is already known, and the XRF measured values were used to determine the recovery efficiency of the target metal from biochar. Metal content quantification and recovery rate analysis involved standard sample preparation, generating calibration plots for the target metals in standard samples, and calculating metal content and recovery efficiency in the biochar samples from gasifier. Calibration and standard sample preparation are described in the following section.

Standard Sample Preparation

For standard samples, we used activated carbon to simulate the biochar. We used a ball mill to pulverize the activated carbon (Figure S3a) ensuring the samples were uniformly ground into powders (~30 μm diameter). Then, known amounts of iron (Fe) powder were

mixed in. The metal and carbon samples were then thoroughly mixed with a chemical binding agent (Elvacite®), exposed to air to dry, and formed into pellets under 25 tons of pressure (Figure S3b). We determined the optimal ratio of the binder to carbon ratio was 1:3. Specifically, 7.8 mL of binder (made of 10 g of Elvacite® in 100 mL of acetone) was determined to be adequate to form the 30 × 5 mm pellets (ca. ~5 g each) for XRF analysis (Figure S3c).

Calibration and Measurement of Known Content of Metals by XRF Analysis

For calibration studies, five standard samples with concentrations of 10, 100, 500, 1000, and 5000 parts per million (ppm) of a specific metal at a time were prepared and mixed with powdered carbon and optimized binder. Figure 4 shows calibration lines from XRF experiments for Fe and Nd.

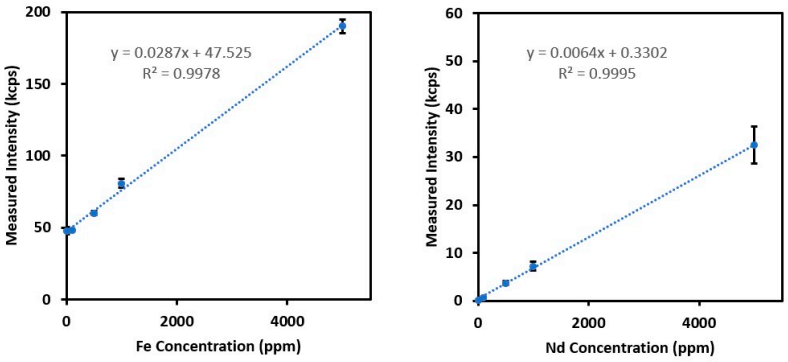

(**a**) (**b**)

Figure 4. Calibration curves of (**a**) Fe, (**b**) Nd plotted using standard samples with concentrations of 10, 100, 500, 1000, and 5000 ppm of corresponding metal + carbon (~3.9 g) + Binder (7.8 mL).

Using these calibrations for each metal, we quantified standard samples to make sure XRF analysis accurately determined metals concentration. Table 4 compares the known amount of metal in several samples against the XRF-measured amounts of metals. The agreement between these values can be improved with additional calibration but is entirely satisfactory for our current needs.

Table 4. The expected content and measured content of metals in five samples.

Expected Sample Concentrations (ppm)	Fe (ppm)	RSD%	Nd (ppm)	RSD%
10	58.00	112.02	11.00	71.86
100	28.88	79.83	62.05	23.24
500	441.27	11.70	528.32	12.75
1000	1162.85	9.60	1080.25	12.80
5000	4967.51	3.24	5019.73	12.02

2.4.2. Quantification of Mean Equivalent Nodule Diameter Distribution on Biochar

Data Analysis Process for Mean Equivalent Nodule Diameter/Fe-Particle Size Distribution

Nodule/Fe-particles were calculated from SEM images, and corresponding EDS images (elemental mapping) were used for locating the nodules containing metal or Fe particles. Due to the non-uniform shape of the nodules/Fe-particles, equivalent nodule/particle sizes were calculated from the two-dimensional projected area (A_p) and by calculating equivalent nodule diameter/particle size (d_e) from the two-dimensional projected nodule/particle area (A_p). Fiji ImageJ V1.53t is used to calculate the two-dimensional projected nodule/particle area (A_p).

$$d_e = \sqrt{\frac{4 \times Ap}{\pi}} \quad (1)$$

As the metal nodule distribution on the biochar surface is not uniform, SEM images were taken on 3–5 different locations of each biochar sample (for both gasifier samples and tube furnace samples). SEM images were selected based on the distinguishability of the nodules and the number of observable nodules. The five best SEM images were selected for each atmospheric condition. Visually distinguishable nodules from each SEM image are selected for size quantification.

Equivalent nodule diameter quantification procedure is discussed below. The same procedure was used for measuring the equivalent nodule diameter for all the SEM images from different experimental conditions. Figure 5a shows the distinguishable nodules (red marked) from a sample SEM image and Figure 5b shows the corresponding elemental mapping of Fe to confirm that marked nodules contain Fe. Figure 6 shows the equivalent nodule diameter distribution as histograms with best-fitted distribution (logistic distribution, $p = 0.079$, significance level: $\alpha = 0.05$, confidence interval: CI = 95%) of nodules from five different sample SEM images. Anderson–Darling (A-D) statistic is used to calculate the p-value for the goodness-of-fit test to determine which distribution best fits the data. Evaluated distributions for the goodness-of-fit test are normal, lognormal, 3-parameter lognormal, Weibull, 3-parameter Weibull, smallest extreme value, largest extreme value, gamma, 3-parameter gamma, logistics, loglogistic, and 3-parameter loglogistic distribution.

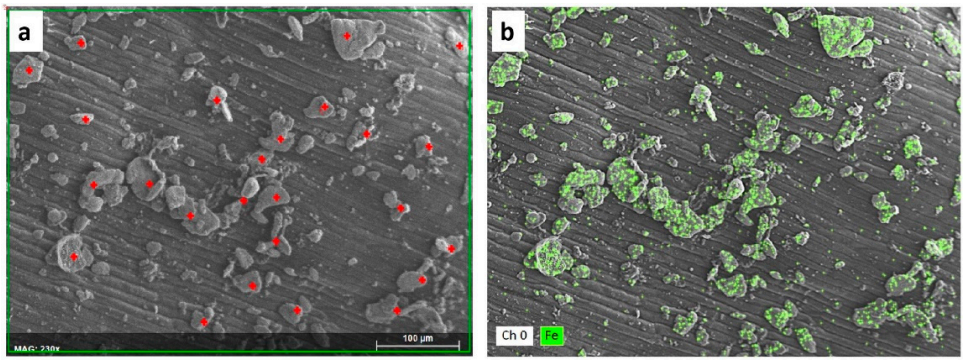

Figure 5. (**a**) Sample SEM image with distinguishable nodules (red marked) to quantify equivalent nodule diameter; (**b**) Fe mapping of the corresponding SEM image (Fe is shown in green). Number of nodules = 25.

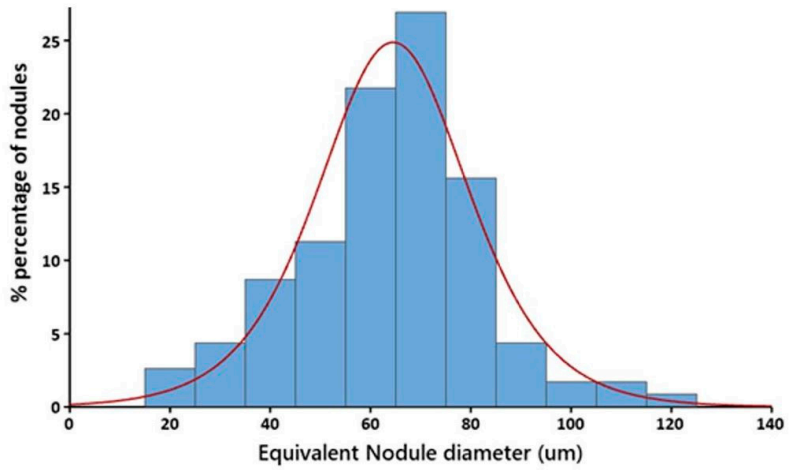

Figure 6. Equivalent nodule diameter distribution of distinguishable nodules from five different SEM images (total nodules: 115).

It should be noted that the discussed sample SEM image and equivalent nodule diameter distribution are from the same experimental conditions.

Elemental Composition Analysis of Selected Nodules

The nodules' elemental compositions were determined using SEM-EDS analysis. Figure 7a shows a sample SEM image with a selected nodule marked as red for elemental composition analysis. Figure 7b shows the EDS energy spectrum of the nodule with atom (%) and chemical composition in the table. The spectrum confirms that the nodule mainly contains the target metal with a composition of FeO.

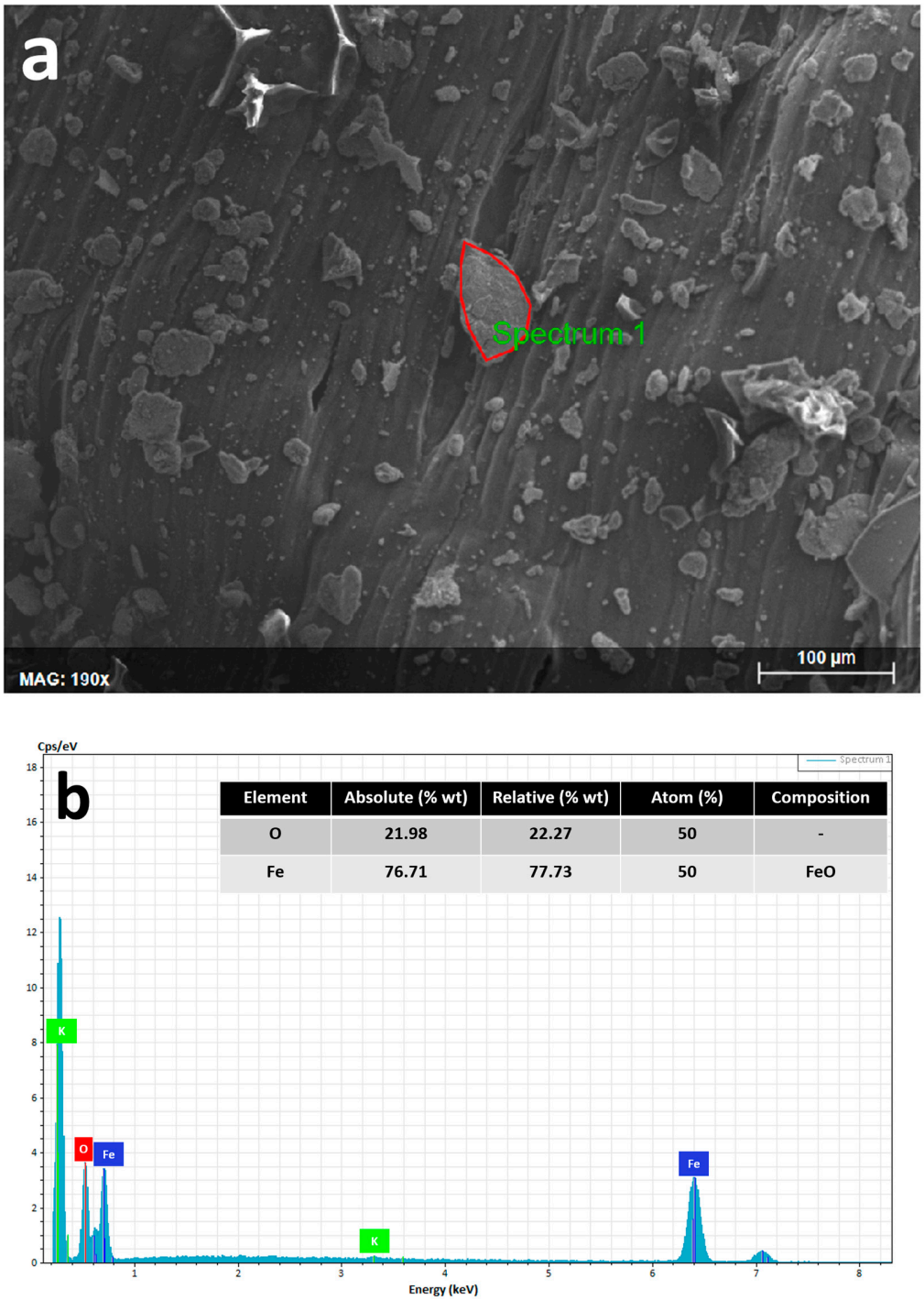

Figure 7. (**a**) Sample SEM Image with selected nodule circled in red; (**b**) EDS spectrum of the nodule with absolute (%wt), relative (%wt), atom (%), and probable chemical composition in the table as surface of iron particles can compose of multiphase oxide layer of FeO, Fe_3O_4, and Fe_2O_3. Elements with <1 atomic %wt are not mentioned.

Baseline Fe and Salt Particle Size Distribution

Mean particle size and particle size distribution are evaluated for Fe and salt particles before exposing them to the gasifier or tube furnace to generate the baseline data. For both Fe and salt particles, particles are mixed with corn separately for SEM-EDS analysis. The size distributions determined by SEM-EDS images are shown in Figure 8a. Raw SEM-EDS images are shown in Figure S4a–f. Fe particles have irregular amorphous appearance (Figure S4a–d) while salt particles have crystalline structures. Figure 8b shows the fitted distribution of the histograms presented in Figure 8a. Fitted distributions are selected through A-D statistic; Fe particles (lognormal distribution, $p = 0.649$, $\alpha = 0.05$, CI = 95%) and salt particles (lognormal distribution, $p = 0.953$, $\alpha = 0.05$, CI = 95%).

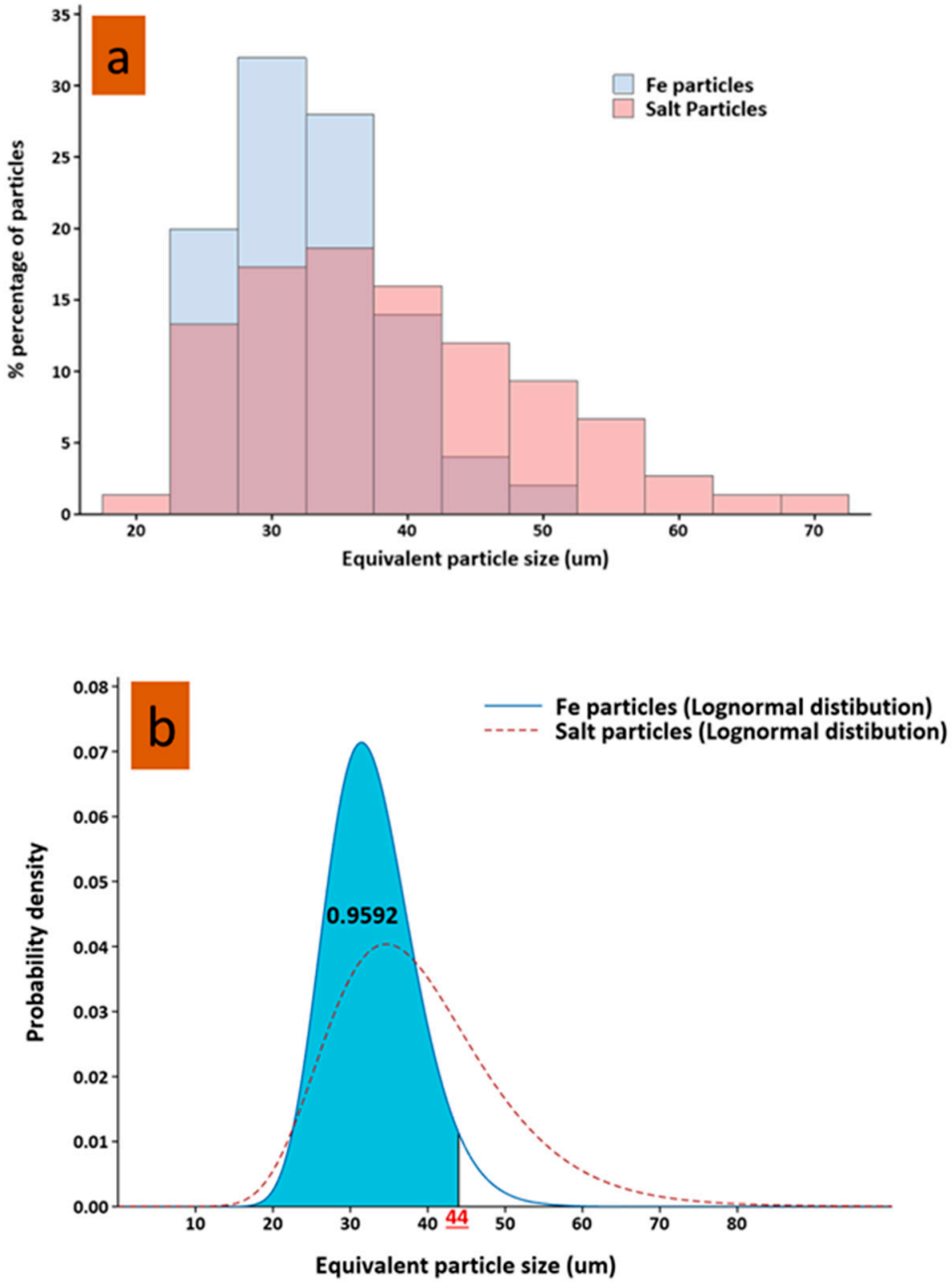

Figure 8. (**a**) Size distributions as histograms; (**b**) probability distributions of Fe and Salt particles.

In addition, Figure 8b also shows the probability of a random Fe particle with equivalent particle size $\leq$ 44 μm which is 0.9592 or 95.92% which follows the manufacturer specification (−325 mesh, 95% particle size < 44 μm).

3. Results and Discussion

3.1. Metal Content Quantification with Possible Recovery Efficiency on Biochar from Gasifier

Having completed the calibration studies (Section Calibration and Measurement of Known Content of Metals by XRF Analysis), work proceeded to synthesize real char samples from the gasification process. Corn was used as a uniform fuel matrix and known amounts of iron powder (~50 g) to 9 kg of the corn were added. Corn seed biomass was sourced from local farms in Iowa, US. Then, the corn and iron were gasified, and several samples of the resulting char were pulverized using a ball mill. Four grams of the resulting powder was used to make pellets similar to Figure S3c suitable for XRF analysis. Table 5 shows the measurement results for three different samples of each metal (see Table S1 for more details). The results are reproducible and show that the method is successful in capturing and quantifying the number of metals present in the gasified char samples.

Table 5. Measured content of metals in 3 biochar samples.

Biochar Samples	Fe (ppm)	Nd (ppm)
Mean	8512	1586
RSD (%)	0.2	9.5
Recovery Percent (%)	34.0	6.3

3.2. Comparison of Mean Equivalent Nodule Diameter, Nodule Morphology and Composition Analysis of Metal Nodules in Different Atmospheric Conditions

3.2.1. Effect of Non-Reducing Atmosphere

The effect of (non)reducing gas phase environment on nodule formation was evaluated by considering three different atmospheric conditions: inert, oxidizing (5% O_2), and ambient (air). Results are detailed in Table 6. The effect of reducing the gas phase environment on nodule formation will be discussed in the next section. Figure 9 shows the comparison of mean equivalent nodule diameter on biochar samples from different non-reducing atmospheres. Compared to the mean equivalent Fe particle size, the reduction in mean equivalent nodule diameter for inert, oxidizing (5% O_2), and ambient (air) atmospheric conditions are 5%, 3%, and 19%, respectively. Games–Howell simultaneous tests for differences of means (Tables S2 and S3) shows that the reduction of the mean equivalent nodule diameter from inert and oxidizing (5% O_2) atmospheric condition are not statistically significant while it is statistically significant for ambient atmosphere (p = 0.832 for inert atmosphere, p = 1.000 for oxidizing-5% O_2 atmosphere and p = 0.005 for ambient atmosphere; α = 0.05, CI = 95%). In addition, no statistically significant changes in mean equivalent nodule diameters are observed by comparing mean equivalent nodule diameter from inert, oxidizing (5% O_2), and ambient (air) atmospheric conditions with each other (Tables S2 and S3). No significant changes in nodule elemental composition are also observed (Figure S5a–f). Evidence of agglomeration between smaller Fe particles (<mean Fe particle size) is observed for inert and oxidizing atmospheric conditions but the size of these agglomerated nodules is not significantly large enough to change the overall equivalent nodule diameter distribution compared to Fe particle size distribution (Figure 10). These signify the effect of the inert and oxidizing atmosphere on metal nodule formation is not significantly different, and it is limited to smaller Fe particles while the larger particles remain unchanged. In addition, the change in oxygen concentration in the experimental atmosphere has no significant effect on metal nodule formation.

The observed reduction in mean equivalent nodule diameter (compared to Fe particle size) from ambient (air) atmospheric conditions can be described through the inherent uncertainty in the biochar collection process and limitations in the selection of biochar

samples for SEM-EDS analysis as this experiment was carried out in pilot scale biomass gasifier connected with a utility-scale boiler. Due to operational limitations of the gasifier, safety concerns, and regulations, the Fe powder and biomass mixture were run for a very short time (~15 min) in the gasifier. In addition, biochar has to pass through the char removal auger (~30 m long) before collecting samples from the char collection outlet. This raises the uncertainty of mixing pure biochar and biochar with Fe powder. Moreover, the selection of samples for SEM-EDS analysis added further uncertainty as a small number of samples was tested (<12 g) from a large collection (2 Kg). This is the key reason to conduct experiments in the tube furnace, to have better control in terms of biochar sample collection processes and analysis, with the capability of performing experiments under different atmospheric conditions.

Table 6. Comparison of mean equivalent nodule diameter in different atmospheric conditions.

Biomass Matrix/ Experiment Conditions	Atmospheric Condition	Number of Nodules Characterized	Mean Equivalent Nodule Diameter/Particle Size (um)	Standard Deviation (um)
Fe particles size	N/A	50	32.91	5.72
Salt particle size	N/A	75	38.81	10.74
2.50%wt Fe + 97.50%wt Corn (From furnace)	Inert (100% Ar)	100	31.25	9.33
2.50%wt Fe + 97.50%wt Corn (From furnace)	Oxidizing Dilute oxygen concentration (95% Ar + 5%O_2)	50	32.17	11.19
0.50%wt Fe + 99.50%wt Corn (From Biomass gasifier)	Oxidizing Ambient oxygen concentration	25	26.64	6.79
2.50%wt Fe + 97.50%wt Corn (N2 + O2 − 20 s) + (N2 + H2 − 80 s) (From furnace)	Oxidizing followed by reducing 95% N2 + 5% O2 and 90% N2 + 10% H2	115	64.05	18.45
2.50%wt Fe + 95.00%wt Corn + 2.50%wt Salt (N2 + O2 − 20 S) +(N2 + H2 − 80 S (From furnace)	Oxidizing followed by reducing 95% N2 + 5% O2 and 90% N2 + 10% H2	125	48.54	23.19

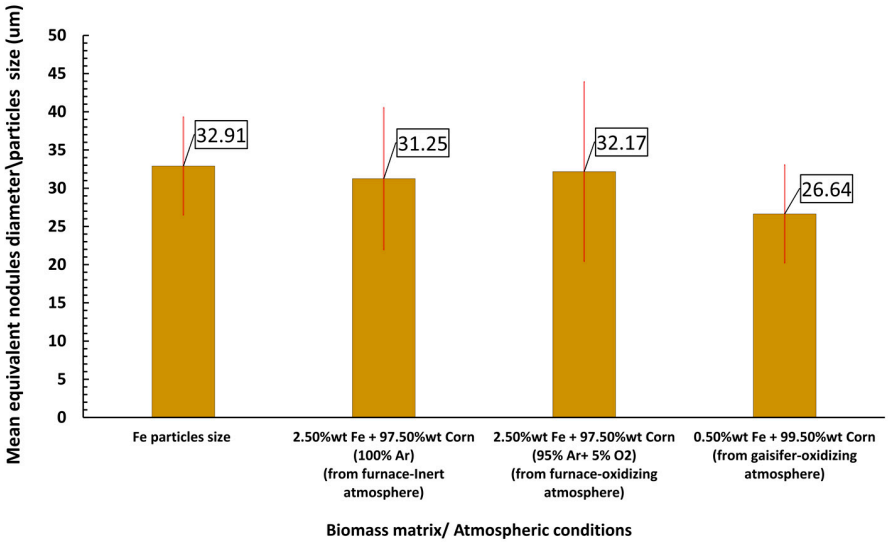

Figure 9. Comparison of mean equivalent nodule diameter in different oxidizing and inert atmospheric conditions. The error bar shows the standard deviation of mean equivalent nodule diameter distinguishable nodules (Table 4) for corresponding atmospheric conditions.

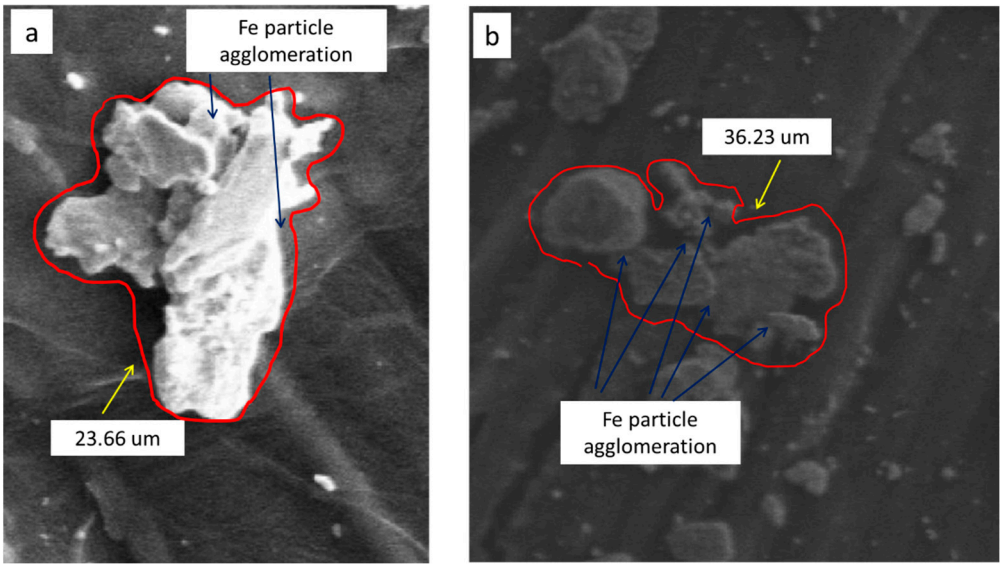

Figure 10. Fe particle agglomeration in (**a**) inert atmosphere, (**b**) oxidizing atmosphere (dilute oxygen concentration).

3.2.2. Effect of Reducing Atmosphere

Experiments show that heating in non-reducing atmospheres has no statistically significant effect on larger metal nodule growth (comparing to Fe particle size). However, agglomeration is observed between smaller Fe particles while the larger particles remain unchanged. The reduction of particle's surface oxide under a reducing atmosphere should enhance the coalescence of particles through particle migration leading to an increase in particle agglomeration and nodule formation [61–70]. Iron powder sintering is commonly carried out in reducing atmospheres such as hydrogen–nitrogen mixtures [66–69]. Thus, the reducing atmosphere used in our work is also expected to favor larger nodule growth. To test this, experiments were conducted in tube furnace with the same metal–biomass composition (2.50%wt Fe + 97.50%wt corn) at a temperature of 1000 ± 100 °C with a gas mixture of 95% HP N_2 + 5% HP O_2 for 20 s, followed by 90% HP N_2 + 10% HP H_2 for 80 s, to provide an oxidizing followed by reducing environment. The mean equivalent nodule diameter of Fe nodules after this process were 64.05 µm ± 18.45 µm (total distinguishable nodules: 125). This corresponds to an approximately 94% increase in the mean equivalent nodule diameter with oxidizing followed by reducing atmosphere compared to mean Fe particle size (32.91 µm), which confirms enhanced sintering between Fe particles. This increase in mean equivalent diameter is also statistically significant comparing to mean Fe particle size ($p < 0.001$, $\alpha = 0.05$, CI = 95%) (Tables S2 and S3). In addition, the changes in mean equivalent nodule diameter between oxidizing followed by reducing atmosphere condition and non-reducing atmosphere condition are statistically significant (for all comparison: $p < 0.001$, $\alpha = 0.05$, CI = 95%) (Tables S2 and S3). Figure 11 shows the comparison of mean equivalent nodule diameter from inert atmosphere, oxidizing atmosphere, and oxidizing followed by reducing atmosphere compared with mean Fe particle size.

Optical microscopy observations of the particle agglomeration sites showed evidence of agglomeration of both large and small particles, as well as inter-nodules agglomeration, which contributes to the larger nodule growth (Figure 12a–d). Overall, experiments in a reducing atmosphere show higher particle coalescence and agglomeration. Increased particle agglomeration sites result in larger nodule growth and an overall significant increase in mean equivalent nodule diameter.

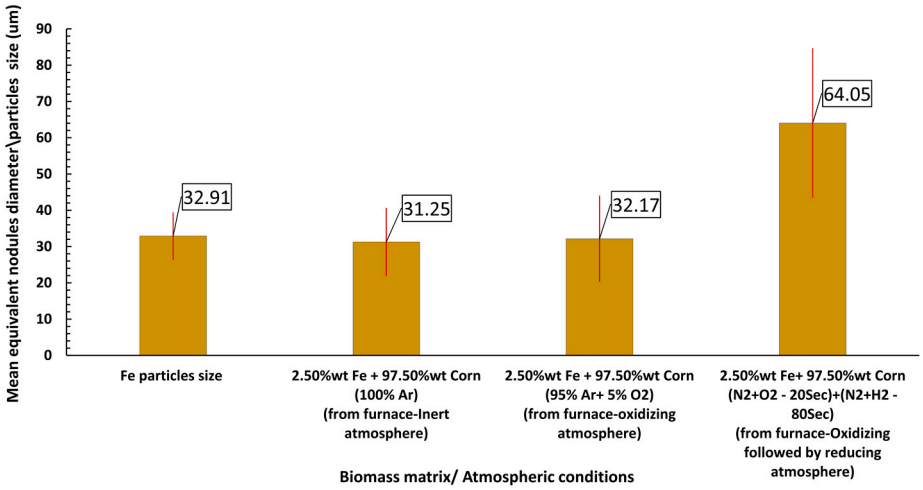

Figure 11. Comparison of mean equivalent nodule diameter from inert atmosphere, oxidizing atmosphere, and oxidizing followed by reducing atmosphere to mean Fe particle size. The error bar shows the standard deviation of mean equivalent nodule diameter of the distinguishable nodules for corresponding atmospheric conditions.

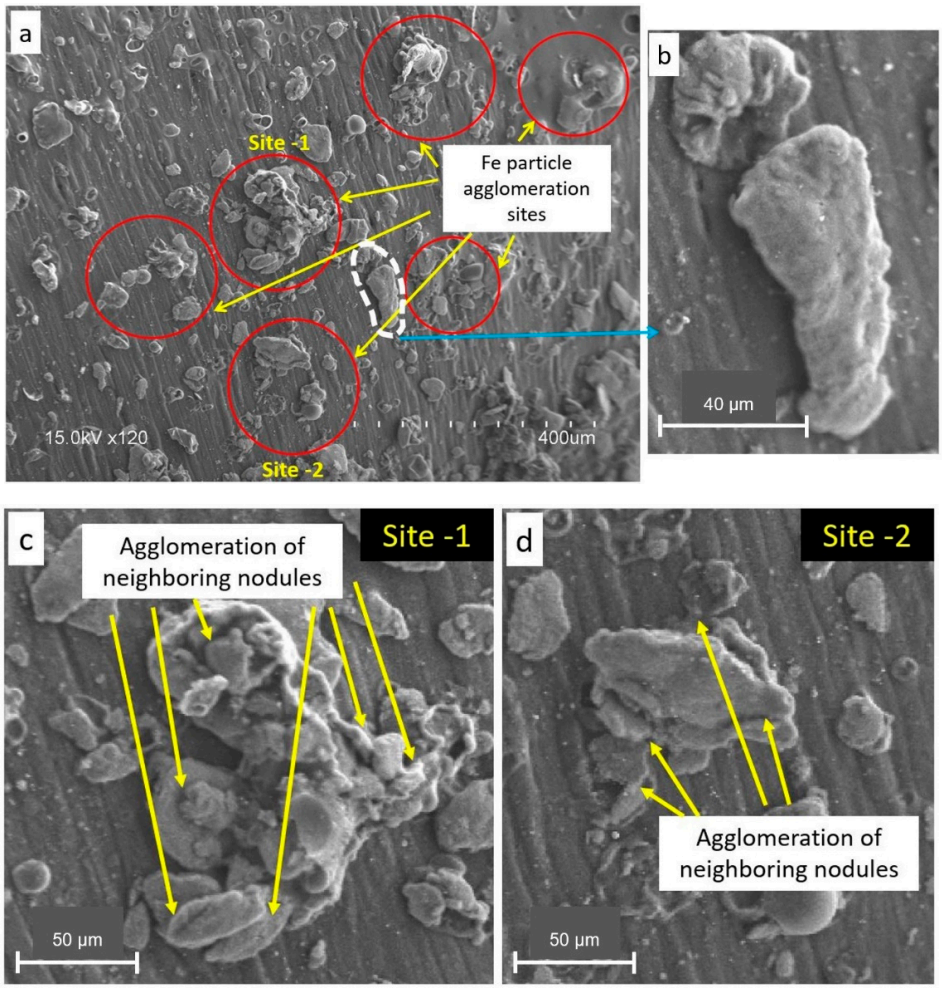

Figure 12. (**a**) Fe particles agglomeration with several particle agglomeration sites (red marked) from experiments in reducing atmosphere; (**b**) enlarged view of a nodule (white marked); (**c**) enlarged view of site-1; (**d**) enlarged view of site-2.

3.2.3. Effect of Reducing Atmosphere with Salt

To further facilitate particle agglomeration, changes to the morphological characteristics of the formed metal nodules by including salt particles with corn/Fe mixtures in the tube furnace were investigated. The addition of salt is expected to enhance particle migration (and hence particle aggregation) by accommodating a liquid phase environment such as molten salt (melting temperature of NaCl: 801 °C < tube furnace/gasifier operating temperature) and enhancing reducing activity [70–74]. These experiments were carried out in the oxidizing followed by the reducing atmosphere regime described above. The only change was the introduction of an additional 2.5% wt. Of salt, this produced a biomass/Fe-particles mixture of 2.50%wt. Fe + 95.00%wt. Corn + 2.50%wt. salt with $N_2 + O_2$ gas mixture flowing for the first 20 s and then an $N_2 + H_2$ gas mixture for 80 s in the tube furnace. The result was an evaluated mean equivalent nodule diameter of 48.54 µm with a standard deviation of 23.19 (total distinguishable nodules: 125). This corresponds to a 46% increase in mean equivalent nodule diameter for oxidizing followed by reducing atmosphere with salt conditions compared to mean Fe particle size. This increase is lower than the oxidizing followed by reducing atmosphere without salt condition. However, this increase in mean equivalent diameter is statistically significant compared to both mean Fe particle size ($p < 0.001$, $\alpha = 0.05$, CI = 95%) and mean salt particle size ($p = 0.002$, $\alpha = 0.05$, CI = 95%). In addition, the changes in mean equivalent nodule diameter between oxidizing followed by reducing atmosphere with the salt condition and the other test conditions are statistically significant (for all comparisons: $p < 0.001$, $\alpha = 0.05$, CI = 95%) (Tables S2 and S3). Figure 13 shows the changes in mean equivalent nodule diameter in oxidizing followed by reducing atmosphere without salt and those with salt in comparison to mean Fe particle size. A higher number of Fe particle agglomeration sites (compared to non-reducing atmospheric conditions) was observed in oxidizing followed by reducing atmosphere with salt and then without salt condition (Figure 14a). No significant change is observed in nodules' elemental composition compared with the reducing atmosphere without salt condition (apart from the presence of some residual sodium, Figure S5e,f). A key distinction of including salt is the nodules' morphological appearance. Most of the nodules have spherical shapes (Figure 14) from oxidizing followed by reducing atmosphere with salt whereas fewer spherical nodules were observed from oxidizing followed by reducing atmosphere without salt (Figure 12).

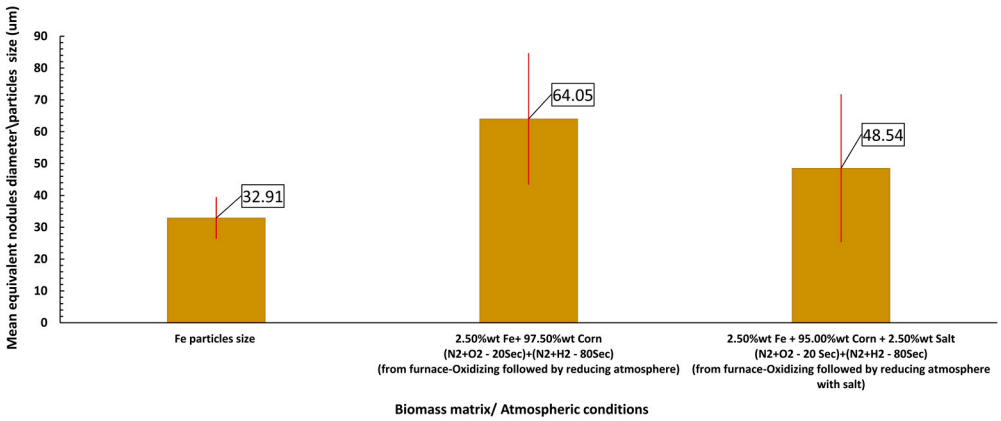

Figure 13. Comparison of mean equivalent nodule diameter from oxidizing followed by reducing atmosphere without salt and oxidizing followed by reducing atmosphere with salt compared to mean Fe particle size. The error bar shows the standard deviation of mean equivalent nodules diameter of the distinguishable nodules for corresponding atmospheric conditions.

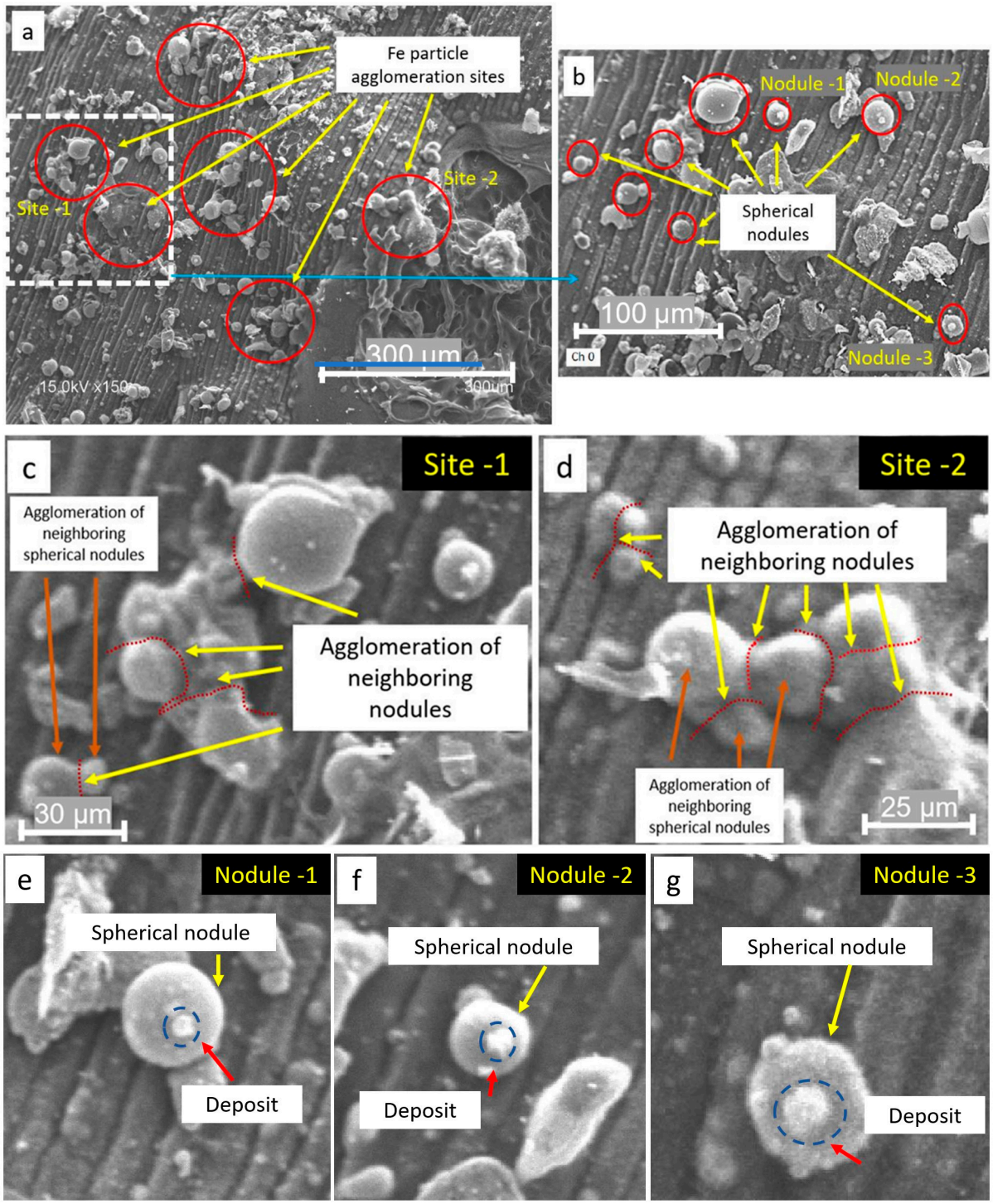

Figure 14. (**a**) Fe particles agglomeration (red marked) from experiments in oxidizing followed by reducing atmosphere with salt; (**b**) enlarged view of an agglomeration site (white dashed line) showing spherical morphology of nodules; (**c**) enlarged view of site-1; (**d**) enlarged view of site-2; (**e**–**g**) enlarged view of nodules 1, 2, and 3 showing deposit (blue dotted lines) on the nodule surface. The red dotted line shows the joint line/connection line of neighboring nodules.

The increasingly spherical nodule shapes signify lower surface energy of the nodules meaning the addition of salt promotes surface energy reduction of the formed nodules. Less surface energy means these nodules have higher thermodynamic stability compared to nodules from oxidizing followed by reducing atmospheres without salt. Agglomer-

ation of spherical nodules is also observed (Figure 14c,d) suggesting enhanced particle migration and nodule agglomeration. Additionally, agglomeration between spherical and non-spherical nodules is observed. The low concentration of sodium (<2%) in nodules confirms that salt particles do not take an active part in nodule formation. This is also evident by comparing the metal nodules' location with the salt particles' location through elemental mapping where no correlation was observed (Figure S6). The observations can be correlated with the "segregation reduction approach" of mineral ore reduction for metal production where halide salts (NaCl, $CaCl_2$, etc.), are used with mineral ore incorporating four key intermediate processes in a cyclic order: (1) HCl formation from the moisture present in the ore, (2) metal chloride vapor formation from metal oxides and HCl, (3) H_2 generation from water vapor reduction by carbon, and (4) reduction of metal-chloride by generated H_2 with the presence of carbon particles forming metal particles and resuming the cycle by generating HCl [73–79]. Similar intermediate processes are present in oxidizing followed by reducing atmosphere with the salt condition which results in the formation of iron chloride vapor from NaCl and H_2 in the presence of carbon particles from biochar, and reduction of iron chloride by H_2 in the presence of carbon particles and subsequent coalescence and aggregation of metal particles through metal vapor accumulation. As biochar has a higher surface area with enhanced catalytic characteristics, the bulk number of metal nodules becoming spherical confirms the presence of similar processes as the "segregation reduction approach of metal ores" [67–73]. Additionally, deposit-type structures on the surface of several spherical nodules are observed. These deposits on the surface of spherical nodules might be considered evidence of the process of metal vapor deposition but further investigation including chemical characterization of these deposits is needed (Figure 14e–g). To summarize, the data suggests that the addition of salt promoted particle migration, increased particle agglomeration, enhanced particle, and nodule coalescence occurrences, and enhanced the stability of formed nodules without significantly changing the nodule composition.

Experimental results presented in the previous sections provide evidence of the formation of larger metal nodules (>mean metal particle size) with oxidizing followed by a reducing atmosphere (with or without salt) as a gasification environment. To predict the probability of larger metal nodule formation compared to mean metal particle size in different atmospheric conditions, probability distribution fitting on the equivalent metal nodule diameter data from different atmospheric conditions is investigated. Anderson–Darling (AD) statistics are used to calculate the p-value for the goodness-of-fit test to determine the best fit distribution for the nodule size data from different atmospheric conditions. Evaluated distributions for the goodness-of-fit test are normal, lognormal, 3-parameter lognormal, Weibull, 3-parameter Weibull, smallest extreme value, largest extreme value, gamma, 3-parameter gamma, logistics, loglogistic, and 3-parameter loglogistic distribution. The summary of the goodness-of-fit test with AD statistics and maximum likelihood (ML) estimates of the distribution parameters are reported in Table S4. Figure S7 shows the probability plots for different distributions.

Figure 15 shows the probability density of the nodule size data from different atmospheric conditions. In Figure 15, vertical dashed lines indicate the mean equivalent nodule diameter from different atmospheric conditions, the arrows show the shifting in mean equivalent nodule diameter compared to mean metal particle size, and the values in parenthesis indicate the percentage changes in mean equivalent nodule diameter compared to mean Fe particles size. The shifting of Fe particle size distribution by different atmospheric conditions due to the process of particle agglomeration and nodule formation can be clearly observed in Figure 15. Metal nodule size from inert and oxidizing atmospheric conditions have similar types of distributions as metal particle size distribution with the slight shifting of the head towards the left tail. The probability density of formed metal nodules from oxidizing followed by reducing atmosphere (with or without salt) shows heavier occurrences in the right tail region due to larger metal nodule sizes through enhance particle agglomeration and increased nodule formation. Figure 16 shows the probability density of

the formation of a random metal nodule having a size larger than the reported mean metal particle size. The results signify that if a metal nodule is formed in oxidizing followed by reducing atmosphere without salt condition, there is ~95% probability that this nodule will be larger than the mean metal particle size. The probability of the formation of metal nodules larger than the mean metal particle size is comparatively lower in inert and oxidizing atmospheric conditions. This signifies there is a high probability that oxidizing followed by a reducing atmosphere will facilitate both large and small particle agglomeration or even nodule agglomeration leading to larger metal nodule growth.

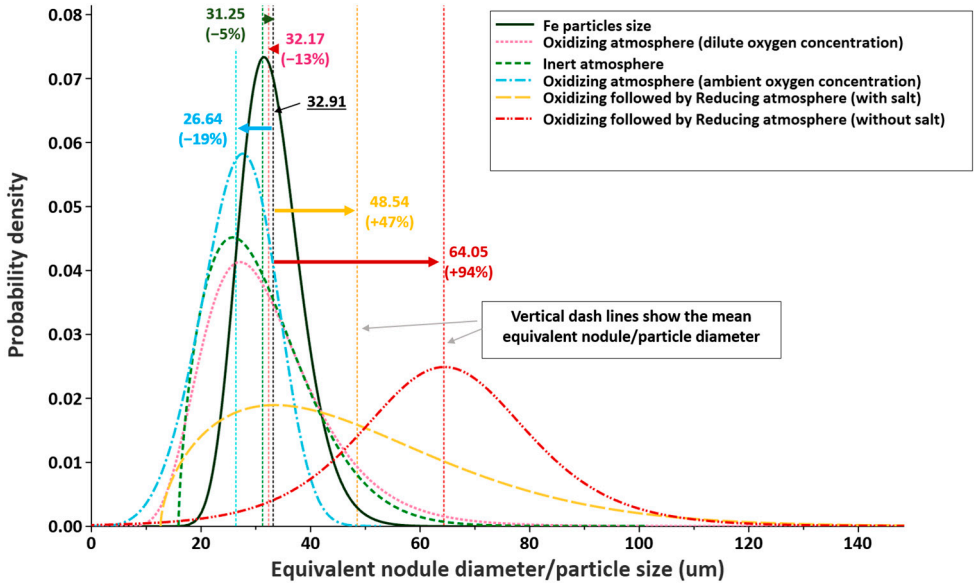

Figure 15. Probability density of equivalent nodule diameter for different atmospheric conditions from fitted distribution. Vertical dash lines show the mean equivalent nodule diameters of corresponding atmospheric condition, arrow signs show the shifting of mean equivalent nodule diameter from mean Fe particle size, and values in parenthesis indicate the percentage changes in mean equivalent nodule diameter compared to mean Fe particles size.

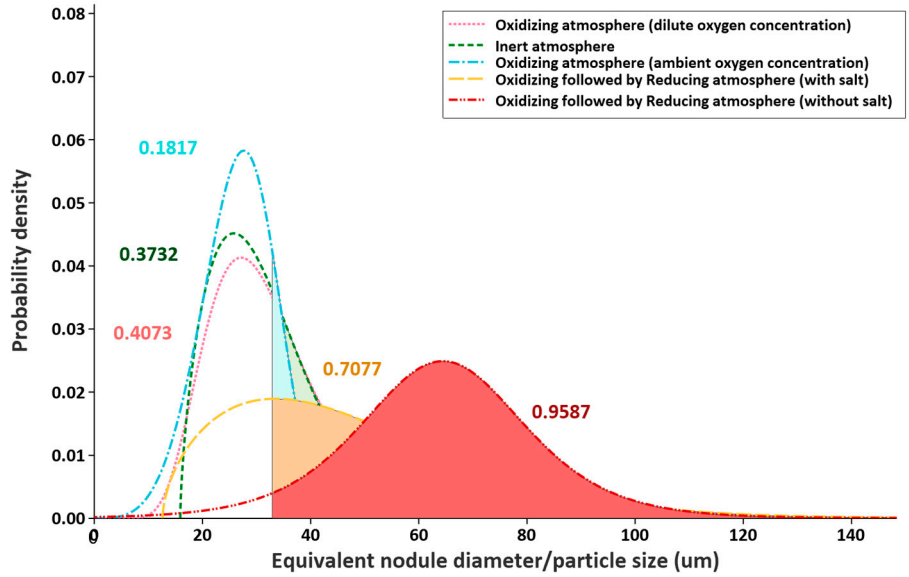

Figure 16. Probability density of equivalent nodule diameter for different atmospheric conditions from fitted distribution. Shaded area shows the probability of a random nodule having an equivalent nodule diameter larger than the mean Fe particle size for the corresponding atmospheric condition.

4. Conclusions

A new pathway to recycle rare earth metals from e-waste through co-gasification with biomass is reported based on the formation of aggregated metal nodules on biochar surfaces where pre-processed e-waste and different gasifier feedstocks (biomass, refused derived fuel, municipal solid waste) might be used as a mixture feedstock for biomass gasifier. Experiments were conducted in both a pilot scale biomass gasifier and a tube furnace with iron powder mixed with corn to simplify the experiments for investigating the effect of different atmospheric conditions (inert, oxidizing, reducing condition) on the formation of metal nodules on biochar surface. Iron powder is used as a representation of the REMs on the e-waste to have a preliminary understanding of the physio-chemical mechanisms responsible for the metal nodule formation on biochar surface and the effect of different atmospheric conditions on metal nodule growth. Experimental observations concluded that sintering is the key mechanism responsible for metal nodule growth through metal particle coalescence and aggregation by migration and diffusion of metal particles to the biochar surface. Mean equivalent diameters of the distinguishable metal nodules are quantified from different reaction conditions and compared with the initial Fe particle size distribution. The morphology and elemental composition of the metal nodules were also compared. Results show that the Fe particle size distributions have not experienced significant changes when exposed to an inert atmosphere or slightly oxidizing (dilute O_2) atmospheres. Though agglomeration between smaller Fe particles (<mean Fe particle size) is observed for inert and oxidizing atmospheric conditions, the size of these agglomerated nodules is not significantly large enough to change the overall equivalent nodule diameter distribution compared to Fe particle size distribution. These observations manifest that the effect of the inert and oxidizing atmosphere on metal nodule formation is not significantly different, and it is limited to smaller Fe particles while the larger particles remain unchanged. In addition, the different oxygen concentrations of the experiment atmosphere have no significant effect on metal nodule formation. However, treating the Fe samples under reducing atmospheres (with or without salt) generally increases the nodule sizes and changes the nodule morphology. Compared with the mean Fe particle size, around 94% and 46% increase in the mean equivalent nodule diameter is observed, respectively, for oxidizing followed by reducing atmosphere without salt and with salt conditions. This increase in formed nodule sizes confirms enhanced agglomeration between Fe particles. In addition, particle agglomeration sites showed evidence of agglomeration of both large and small particles as well as inter-nodules agglomeration which contributes to the larger nodule growth. This increase in mean equivalent diameter is also statistically significant compared to both mean Fe particle size and mean equivalent nodule diameter from non-reducing atmospheres. The key distinction between the metal nodules formed without salt and with the salt condition is their morphological appearance. Most of the nodules have spherical shapes from oxidizing followed by reducing atmosphere with salt condition whereas fewer spherical nodules were observed from oxidizing followed by reducing atmosphere without salt. The increasingly spherical nodule shapes signify lower surface energy of the nodules meaning the addition of salt promotes surface energy reduction of the formed nodules while not taking an active part in nodule formation. This is confirmed by the elemental mapping where no correlation was observed between the metal nodules' location and with salt particles' location. Finally, probability distribution fitting on the equivalent metal nodule diameter data from different atmospheric conditions revealed distinct distributions and their corresponding shifting relative to Fe particle size distribution.

Additional studies to investigate the effects of different temperature programs, other (reducing) atmospheric conditions, and the effect of "endo" gases e.g., CO, CO_2, H_2O, and their concentration on nodule formation and growth rate should be conducted. In addition, the effects of residence time inside the tube furnace and heating rate as well as the characterization of metal nodule biochar surface interactions and biochar's physio-chemical characteristics on metal nodule growth will be investigated. Finally, optimized key operating parameters and atmospheric conditions will be correlated with both thermo-

physical and chemical characteristics of REMs and will be utilized to characterize REMs' nodule formation on biochar.

Supplementary Materials: The following supporting information can be downloaded at: https://www.mdpi.com/article/10.3390/en15239141/s1, Figure S1: Schematic of the gasifier with two stage metal powder dosing system; Figure S2: Schematic of the experiment set up with tube furnace; Figure S3: (a) Activated carbon in the ball mill cylinder is being mounted on the ball mill; (b) press machine; (c) carbon + iron metal pellet; Figure S4: (a) SEM image of raw Fe powder; (b) elemental mapping of raw Fe powder; (c) SEM image of mixture of Fe powder and corn; (d) elemental mapping of mixture of Fe powder and corn; (e) SEM image of mixture of salt and corn; (f) elemental mapping of mixture of salt and corn; Figure S5: Elemental composition of selected nodules/particles (marked as red) of (a) raw Fe particles (F1), and from different atmospheric conditions: (b) inert; (c) oxidizing (dilute oxygen concentration); (d) oxidizing (ambient oxygen concentration); (e) reducing atmosphere; (f) reducing atmosphere with salt; Figure S6: (a) SEM image; (b) corresponding Fe location; (c) Fe mapping; (d) Na mapping; (e) K mapping; (f) Cl mapping for one of the SEM images for experiment condition no-4 (2.50% Fe + 95.00% corn + 2.50% salt (N_2 + O_2 − 20 s) +(N_2 + H_2 − 80 s)); Figure S7: Probability plots for different fitted distributions; Table S1: Measured content of metals in 3 biochar samples; Table S2: Grouping information using the Games–Howell method with 95% confidence interval; Table S3: Games-Howell Simultaneous Tests for Differences of Means (significance level: α = 0.05, confidence interval = 95%); Table S4: Anderson–Darling statistic for goodness-of-fit test and maximum likelihood (ML) estimates of distribution parameters (significance level: α = 0.05, confidence interval = 95%).

Author Contributions: Conceptualization, S.K.S. and A.R.; formal analysis, A.S.M.S.P. and R.O.-S.; funding acquisition, S.K.S. and A.R.; investigation, A.S.M.S.P., R.O.-S. and T.S.; methodology, T.S., S.K.S. and A.R.; project administration, S.K.S. and A.R.; supervision, S.K.S. and A.R.; writing—original draft, A.S.M.S.P. and R.O.-S.; writing—review and editing, A.S.M.S.P., R.O.-S., S.K.S. and A.R.; A.S.M.S.P. and R.O.-S. contributed equally to this work. All authors have read and agreed to the published version of the manuscript.

Funding: This research was funded by KBIH Foundation, the US Department of Transportation through a Mid-American Transportation Center (MATC) grant with USDOT UTC grant number 69A3551747107, and the University of Iowa.

Data Availability Statement: The data that support the findings of this study are available from the corresponding author upon request.

Acknowledgments: The authors gratefully acknowledge the following: University of Iowa Department of Mechanical Engineering and Department of Chemistry, and Brad Swearingen, Powerplant manager at Oakdale Utility Power Plant, for facilitating experiments in biomass gasifier. Emily Finzel from the Earth and Environmental Science Department, University of Iowa for training and providing the team with the ball mill and press machine for the XRF analysis. The Materials Analysis, Testing, and Fabrication (MATFab) Facility at University of Iowa. Lou Messerle for providing our team with access to a tube furnace.

Conflicts of Interest: The authors declare no conflict of interest. The funders had no role in the design of the study; in the collection, analyses, or interpretation of data; in the writing of the manuscript, or in the decision to publish the results.

References

1. Balaram, V. Rare earth elements: A review of applications, occurrence, exploration, analysis, recycling, and environmental impact. *Geosci. Front.* **2019**, *10*, 1285–1303. [CrossRef]
2. Eggert, R.G. Minerals go critical. *Nat. Chem.* **2011**, *3*, 688–691. [CrossRef] [PubMed]
3. Pistilli, M. Top 10 Countries for Rare Earth Metal Production (Updated 2022). 2022. Available online: https://investingnews.com/daily/resource-investing/critical-metals-investing/rare-earth-investing/rare-earth-metal-production/ (accessed on 28 August 2022).
4. Binnemans, K.; Jones, P.T.; Blanpain, B.; Van Gerven, T.; Yang, Y.; Walton, A.; Buchert, M. Recycling of rare earths: A critical review. *J. Clean. Prod.* **2013**, *51*, 1–22. [CrossRef]
5. Schlesinger, M.E. *Aluminum Recycling*; CRC Press: Boca Raton, FL, USA, 2006.
6. Björkman, B.; Samuelsson, C. Recycling of steel. In *Handbook of Recycling*; Elsevier: Amsterdam, The Netherlands, 2014; pp. 65–83.

7. Lee, J.C.K.; Wen, Z. Pathways for greening the supply of rare earth elements in China. *Nat. Sustain.* **2018**, *1*, 598–605. [CrossRef]
8. Jones, P.T.; Van Gerven, T.; Van Acker, K.; Geysen, D.; Binnemans, K.; Fransaer, J.; Blanpain, B.; Mishra, B.; Apelian, D. CR3: Cornerstone to the sustainable inorganic materials management (SIM2) research program at KU Leuven. *JOM* **2011**, *63*, 14–15. [CrossRef]
9. Schüler, D.; Buchert, M.; Liu, R.; Dittrich, S.; Merz, C. Study on rare earths and their recycling. *Öko-Inst. Darmstadt* **2011**, *49*, 30–40.
10. Brunner, P.H. Urban Mining A Contribution to Reindustrializing the City. *J. Ind. Ecol.* **2011**, *15*, 339–341. [CrossRef]
11. Cheng, H.; Chen, C.; Wu, S.; Mirza, Z.A.; Liu, Z. Emergy evaluation of cropping, poultry rearing, and fish raising systems in the drawdown zone of Three Gorges Reservoir of China. *J. Clean. Prod.* **2017**, *144*, 559–571. [CrossRef]
12. Sharma, T. *Biochar and Other Properties Resulting from the Gasification and Combustion of Biomass with Different Components in Mechanical Engineering*; University of Iowa: Iowa City, IA, USA, 2019; p. 141.
13. Sharma, T. *Gasification and Combustion of Corn Kernels in a Pilot Scale System*; University of Iowa: Iowa City, IA, USA, 2015.
14. Sun, Z.; Xiao, Y.; Agterhuis, H.; Sietsma, J.; Yang, Y. Recycling of metals from urban mines—A strategic evaluation. *J. Clean. Prod.* **2016**, *112*, 2977–2987. [CrossRef]
15. Alam, M.A.; Zuga, L.; Pecht, M.G. Economics of rare earth elements in ceramic capacitors. *Ceram. Int.* **2012**, *38*, 6091–6098. [CrossRef]
16. Falconnet, P. The economics of rare earths. *J. Less Common Met.* **1985**, *111*, 9–15. [CrossRef]
17. Sethurajan, M.; van Hullebusch, E.D.; Fontana, D.; Akcil, A.; Deveci, H.; Batinic, B.; Leal, J.; Gasche, T.A.; Kucuker, M.A.; Kuchta, K.; et al. Recent advances on hydrometallurgical recovery of critical and precious elements from end of life electronic wastes—A review. *Crit. Rev. Environ. Sci. Technol.* **2019**, *49*, 212–275. [CrossRef]
18. Kim, D.; Powell, L.; Delmau, L.H.; Peterson, E.S.; Herchenroeder, J.; Bhave, R.R. A supported liquid membrane system for the selective recovery of rare earth elements from neodymium-based permanent magnets. *Sep. Sci. Technol.* **2016**, *51*, 1716–1726. [CrossRef]
19. Tunsu, C.; Petranikova, M.; Gergorić, M.; Ekberg, C.; Retegan, T. Reclaiming rare earth elements from end-of-life products: A review of the perspectives for urban mining using hydrometallurgical unit operations. *Hydrometallurgy* **2015**, *156*, 239–258. [CrossRef]
20. Omodara, L.; Pitkäaho, S.; Turpeinen, E.-M.; Saavalainen, P.; Oravisjärvi, K.; Keiski, R.L. Recycling and substitution of light rare earth elements, cerium, lanthanum, neodymium, and praseodymium from end-of-life applications—A review. *J. Clean. Prod.* **2019**, *236*, 117573. [CrossRef]
21. Dutta, T.; Kim, K.-H.; Uchimiya, M.; Kwon, E.E.; Jeon, B.-H.; Deep, A.; Yun, S.-T. Global demand for rare earth resources and strategies for green mining. *Environ. Res.* **2016**, *150*, 182–190. [CrossRef]
22. Isildar, A.; Rene, E.R.; van Hullebusch, E.D.; Lens, P.N.L. Electronic waste as a secondary source of critical metals: Management and recovery technologies. *Resour. Conserv. Recycl.* **2018**, *135*, 296–312. [CrossRef]
23. Magoda, K.; Mekuto, L. Biohydrometallurgical Recovery of Metals from Waste Electronic Equipment: Current Status and Proposed Process. *Recycling* **2022**, *7*, 67. [CrossRef]
24. Jowitt, S.M.; Werner, T.T.; Weng, Z.; Mudd, G.M. Recycling of the rare earth elements. *Curr. Opin. Green Sustain. Chem.* **2018**, *13*, 1–7. [CrossRef]
25. Kim, D.; Powell, L.E.; Delmau, L.H.; Peterson, E.S.; Herchenroeder, J.; Bhave, R.R. Selective Extraction of Rare Earth Elements from Permanent Magnet Scraps with Membrane Solvent Extraction. *Environ. Sci. Technol.* **2015**, *49*, 9452–9459. [CrossRef]
26. Tan, Q.; Deng, C.; Li, J. Innovative Application of Mechanical Activation for Rare Earth Elements Recovering: Process Optimization and Mechanism Exploration. *Sci. Rep.* **2016**, *6*, 19961. [CrossRef] [PubMed]
27. Karal, E.; Kucuker, M.A.; Demirel, B.; Copty, N.K.; Kuchta, K. Hydrometallurgical recovery of neodymium from spent hard disk magnets: A life cycle perspective. *J. Clean. Prod.* **2021**, *288*, 125087. [CrossRef]
28. Reck, B.K.; Graedel, T.E. Challenges in Metal Recycling. *Science* **2012**, *337*, 690–695. [CrossRef] [PubMed]
29. Cheisson, T.; Schelter, E.J. Rare earth elements: Mendeleev's bane, modern marvels. *Science* **2019**, *363*, 489–493. [CrossRef] [PubMed]
30. Zhang, S.; Ding, Y.; Liu, B.; Pan, D.; Chang, C.-C.; Volinsky, A.A. Challenges in legislation, recycling system and technical system of waste electrical and electronic equipment in China. *Waste Manag.* **2015**, *45*, 361–373. [CrossRef] [PubMed]
31. Hagelüken, C.; Lee-Shin, J.U.; Carpentier, A.; Heron, C. The EU Circular Economy and Its Relevance to Metal Recycling. *Recycling* **2016**, *1*, 242–253. [CrossRef]
32. Li, F.-Q.; Wang, P.; Chen, W.; Wen, B.-J.; Dai, T. Exploring recycling potential of rare, scarce, and scattered metals: Present status and future directions. *Sustain. Prod. Consum.* **2022**, *30*, 988–1000. [CrossRef]
33. Tunsu, C.; Retegan, T. Hydrometallurgical Processes for the Recovery of Metals from WEEE. In *WEEE Recycling*; Elsevier: Amsterdam, The Netherlands, 2016; pp. 139–175.
34. Kumar, V.; Jha, M.K.; Kumari, A.; Panda, R.; Kumar, J.R.; Lee, J.Y. Recovery of Rare Earth Metals (REMs) from Primary and Secondary Resources: A Review. 2014. Available online: http://eprints.nmlindia.org/6852 (accessed on 24 August 2022).
35. Faramarzi, M.A.; Mogharabi-Manzari, M.; Brandl, H. Bioleaching of metals from wastes and low-grade sources by HCN-forming microorganisms. *Hydrometallurgy* **2020**, *191*, 105228. [CrossRef]
36. Habibi, A.; Kourdestani, S.S.; Hadadi, M. Biohydrometallurgy as an environmentally friendly approach in metals recovery from electrical waste: A review. *Waste Manag. Res. J. Sustain. Circ. Econ.* **2020**, *38*, 232–244. [CrossRef]

37. Itoh, M.; Miura, K.; Machida, K.-I. Novel rare earth recovery process on Nd–Fe–B magnet scrap by selective chlorination using NH4Cl. *J. Alloys Compd.* **2009**, *477*, 484–487. [CrossRef]
38. Uda, T. Recovery of Rare Earths from Magnet Sludge by FeCl2. *Mater. Trans.* **2002**, *43*, 55–62. [CrossRef]
39. Shimizu, R.; Sawada, K.; Enokida, Y.; Yamamoto, I. Supercritical fluid extraction of rare earth elements from luminescent material in waste fluorescent lamps. *J. Supercrit. Fluids* **2005**, *33*, 235–241. [CrossRef]
40. Yao, Y.; Farac, N.F.; Azimi, G. Supercritical Fluid Extraction of Rare Earth Elements from Nickel Metal Hydride Battery. *ACS Sustain. Chem. Eng.* **2017**, *6*, 1417–1426. [CrossRef]
41. Deshmane, V.G.; Islam, S.Z.; Bhave, R.R. Selective Recovery of Rare Earth Elements from a Wide Range of E-Waste and Process Scalability of Membrane Solvent Extraction. *Environ. Sci. Technol.* **2019**, *54*, 550–558. [CrossRef]
42. Bian, Y.; Guo, S.; Jiang, L.; Liu, J.; Tang, K.; Ding, W. Recovery of Rare Earth Elements from NdFeB Magnet by VIM-HMS Method. *ACS Sustain. Chem. Eng.* **2015**, *4*, 810–818. [CrossRef]
43. Cui, J.; Zhang, L. Metallurgical recovery of metals from electronic waste: A review. *J. Hazard. Mater.* **2008**, *158*, 228–256. [CrossRef]
44. Lehmann, J.; Joseph, S. *Biochar for Environmental Management: Science, Technology and Implementation*; Routledge: London, UK, 2015.
45. Amin, F.R.; Huang, Y.; He, Y.; Zhang, R.; Liu, G.; Chen, C. Biochar applications and modern techniques for characterization. *Clean Technol. Environ. Policy* **2016**, *18*, 1457–1473. [CrossRef]
46. Bolan, N.; Hoang, S.A.; Beiyuan, J.; Gupta, S.; Hou, D.; Karakoti, A.; Joseph, S.; Jung, S.; Kim, K.-H.; Kirkham, M.; et al. Multifunctional applications of biochar beyond carbon storage. *Int. Mater. Rev.* **2022**, *67*, 150–200. [CrossRef]
47. Sharma, T.; Ratner, A. Analysis and Characterization of Metallic Nodules on Biochar from Single-Stage Downdraft Gasification. *Processes* **2021**, *9*, 533. [CrossRef]
48. German, R.M. *Powder Metallurgy Science*; Metal Powder Industries Federation: Princeton, NJ, USA, 1984.
49. Dietze, E.M.; Abild-Pedersen, F.; Plessow, P.N. Comparison of Sintering by Particle Migration and Ripening through First-Principles-Based Simulations. *J. Phys. Chem. C* **2018**, *122*, 26563–26569. [CrossRef]
50. Yoon, H.-S.; Kim, C.-J.; Chung, K.W.; Lee, J.-Y.; Shin, S.M.; Lee, S.-J.; Joe, A.-R.; Lee, S.-I.; Yoo, S.-J. Leaching kinetics of neodymium in sulfuric acid of rare earth elements (REE) slag concentrated by pyrometallurgy from magnetite ore. *Korean J. Chem. Eng.* **2014**, *31*, 1766–1772. [CrossRef]
51. Binnemans, K.; Jones, P.T.; Blanpain, B.; Van Gerven, T.; Pontikes, Y. Towards zero-waste valorisation of rare-earth-containing industrial process residues: A critical review. *J. Clean. Prod.* **2015**, *99*, 17–38. [CrossRef]
52. Liu, P.; Chen, G.-F. *Porous Materials: Processing and Applications*; Elsevier: Amsterdam, The Netherlands, 2014.
53. Campbell, C.T. The Energetics of Supported Metal Nanoparticles: Relationships to Sintering Rates and Catalytic Activity. *Accounts Chem. Res.* **2013**, *46*, 1712–1719. [CrossRef]
54. Campbell, C.T.; Sellers, J.R.V. Anchored metal nanoparticles: Effects of support and size on their energy, sintering resistance and reactivity. *Faraday Discuss.* **2013**, *162*, 9–30. [CrossRef]
55. Dai, Y.; Lu, P.; Cao, Z.; Campbell, C.T.; Xia, Y. The physical chemistry and materials science behind sinter-resistant catalysts. *Chem. Soc. Rev.* **2018**, *47*, 4314–4331. [CrossRef] [PubMed]
56. Glushkov, D.; Nyashina, G.; Shvets, A.; Pereira, A.; Ramanathan, A. Current Status of the Pyrolysis and Gasification Mechanism of Biomass. *Energies* **2021**, *14*, 7541. [CrossRef]
57. Ahmed, M.B.; Zhou, J.L.; Ngo, H.H.; Guo, W.; Chen, M. Progress in the preparation and application of modified biochar for improved contaminant removal from water and wastewater. *Bioresour. Technol.* **2016**, *214*, 836–851. [CrossRef]
58. Liu, Z.; Xu, Z.; Xu, L.; Buyong, F.; Chay, T.C.; Li, Z.; Cai, Y.; Hu, B.; Zhu, Y.; Wang, X. Modified biochar: Synthesis and mechanism for removal of environmental heavy metals. *Carbon Res.* **2022**, *1*, 8. [CrossRef]
59. Bogart, J.A.; Cole, B.E.; Boreen, M.A.; Lippincott, C.A.; Manor, B.C.; Carroll, P.J.; Schelter, E.J. Accomplishing simple, solubility-based separations of rare earth elements with complexes bearing size-sensitive molecular apertures. *Proc. Natl. Acad. Sci. USA* **2016**, *113*, 14887–14892. [CrossRef]
60. Bogart, J.A.; Lippincott, C.A.; Carroll, P.J.; Schelter, E.J. An Operationally Simple Method for Separating the Rare-Earth Elements Neodymium and Dysprosium. *Angew. Chem.* **2015**, *127*, 8340–8343. [CrossRef]
61. Höganäs AB Laboratory. Material and Powder Properties. In *Höganäs Handbook for Sintered Components*; Höganäs AB Laboratory: Höganäs, Sweden, 2013.
62. Wynblatt, P.; Gjostein, N.A. Supported metal crystallites. *Prog. Solid State Chem.* **1975**, *9*, 21. [CrossRef]
63. McCaldin, J.; Somorjai, G.; Mataré, H.F. Progress in Solid State Chemistry. *J. Electrochem. Soc.* **1977**, *124*, 219C. [CrossRef]
64. Mitchell, C.; Howard, A.; Carney, M.; Egdell, R. Direct observation of behaviour of Au nanoclusters on TiO2(110) at elevated temperatures. *Surf. Sci.* **2001**, *490*, 196–210. [CrossRef]
65. Parker, S.C.; Campbell, C.T. Kinetic model for sintering of supported metal particles with improved size-dependent energetics and applications to Au on TiO 2 (110). *Phys. Rev. B* **2007**, *75*, 035430. [CrossRef]
66. Zakharova, E.; Dzidziguri, E.; Sidorova, E.; Vasiliev, A.; Pelevin, I.; Ozherelkov, D.; Nalivaiko, A.; Gromov, A. Characterization of Multiphase Oxide Layer Formation on Micro and Nanoscale Iron Particles. *Metals* **2020**, *11*, 12. [CrossRef]
67. Parkinson, G.S. Iron oxide surfaces. *Surf. Sci. Rep.* **2016**, *71*, 272–365. [CrossRef]
68. Jozwiak, W.; Kaczmarek, E.; Maniecki, T.; Ignaczak, W.; Maniukiewicz, W. Reduction behavior of iron oxides in hydrogen and carbon monoxide atmospheres. *Appl. Catal. A Gen.* **2007**, *326*, 17–27. [CrossRef]

69. Lin, H.-Y.; Chen, Y.-W.; Li, C. The mechanism of reduction of iron oxide by hydrogen. *Thermochim. Acta* **2003**, *400*, 61–67. [CrossRef]
70. Cornell, R.M.; Schwertmann, U. *The Iron Oxides: Structure, Properties, Reactions, Occurrences, and Uses*; Wiley-Vch: Weinheim, Germany, 2003; Volume 664.
71. Bagaria, H.G.; Yoon, K.Y.; Neilson, B.M.; Cheng, V.; Lee, J.H.; Worthen, A.J.; Xue, Z.; Huh, C.; Bryant, S.L.; Bielawski, C.W.; et al. Stabilization of Iron Oxide Nanoparticles in High Sodium and Calcium Brine at High Temperatures with Adsorbed Sulfonated Copolymers. *Langmuir* **2013**, *29*, 3195–3206. [CrossRef]
72. Zhou, S.; Wei, Y.; Li, B.; Wang, H.; Ma, B.; Wang, C. Mechanism of sodium chloride in promoting reduction of high-magnesium low-nickel oxide ore. *Sci. Rep.* **2016**, *6*, 29061. [CrossRef]
73. Yu, D.; Paktunc, D. Direct Production of Ferrochrome by Segregation Reduction of Chromite in the Presence of Calcium Chloride. *Metals* **2018**, *8*, 69. [CrossRef]
74. Moulden, J.; Taplin, B. Improvements in or Relating to the Heat Treatment of Oxidized Copper Ores. British Patent 250991, 1924.
75. Kwatara, M.; Tayabally, J.; Peek, E.; Schonewille, R. Segregation Roasting of a Saprolitic Laterite Ore: An Experimental Investigation. In *EPD Congress 2011*; Wiley Online Library: Hoboken, NJ, USA, 2011.
76. Mehrotra, S.; Srinivasan, V. Extraction of nickel from an Indian laterite by segregation roasting. *Trans. Inst. Min. Metall. C* **1994**, *103*, 60–88.
77. Zhou, S.; Wei, Y.; Li, B.; Wang, H.; Ma, B.; Wang, C. Chloridization and Reduction Roasting of High-Magnesium Low-Nickel Oxide Ore Followed by Magnetic Separation to Enrich Ferronickel Concentrate. *Met. Mater. Trans. A* **2016**, *47*, 145–153. [CrossRef]
78. Bhattacharya, M. Reaction mechanism and thermodynamics of segregation roasting of iron oxide. *Int. J. Miner. Process. Extr. Metall.* **2016**, *1*, 64–69.
79. Hernandez, V.; Peake, K.; Dalvi, A.; Brown, R.; Olurin, J.; O'Farrell, T.; Zhou, M.; Liu, B.; Cameron, I. *Process Development of a New DRI Technology for Oolitic Iron Ores*; AISTech Proceedings; Association for Iron & Steel Technology: Pittsburgh, PA, USA, 2013; pp. 519–526.